



# Application of the MEGNO technique to the dynamics of Jovian irregular satellites

T. C. Hinse,<sup>1,2</sup>★ A. A. Christou,<sup>1</sup> J. L. A. Alvarellos<sup>3</sup> and K. Goździewski<sup>4</sup>

<sup>1</sup>Armagh Observatory, College Hill, Armagh BT61 9DG

<sup>2</sup>Niels Bohr Institute, University of Copenhagen, Juliane Maries Vej 30, Copenhagen Ø, 2100, Denmark

<sup>3</sup>Space Systems/Loral MS G-76, 3825 Fabian Way, Palo Alto, CA 94303, USA

<sup>4</sup>Nicolaus Copernicus University, Gagarin Str. 11, 87-100 Toruń, Poland

Accepted 2010 January 7. Received 2010 January 6; in original form 2009 July 22

## ABSTRACT

We apply the Mean Exponential Growth Factor of Nearby Orbits (MEGNO) technique to the dynamics of Jovian irregular satellites. The MEGNO indicator is a practical numerical tool to distinguish between quasi-periodic and chaotic structures in phase space of a given dynamical system. The MEGNO indicator is used to generate a mapping of relevant phase-space regions occupied by observed Jovian irregular satellites. The construction of MEGNO maps of the Jovian phase-space region within its Hill-sphere is addressed and the obtained results are compared with previous studies regarding the dynamical stability of irregular satellites. Since this is the first time the MEGNO technique is applied to study the dynamics of irregular satellites, we provide a review of the MEGNO theory and illustrate basic properties. We consider the elliptic restricted three-body problem in which Jupiter is orbited by a massless test satellite subject to solar gravitational perturbations. The equations of motion of the system are integrated numerically and the MEGNO indicator computed from the system's variational equations. A large set of initial conditions is studied to generate the MEGNO maps. The chaotic nature of initial conditions is demonstrated by studying a quasi-periodic orbit and a chaotic orbit. As a result, we establish the existence of several high-order mean-motion resonances (MMR) detected for retrograde orbits along with other interesting dynamical features related to various dynamical resonances. The computed MEGNO maps allow us to differentiate qualitatively between chaotic and quasi-periodic regions of the irregular satellite phase space within a relatively short integration time of 60 000 yr for each orbit. By comparing with previous published results, we can establish a correlation between chaotic regions and corresponding regions of orbital instability. Based on our results, we hypothesize on the possibility of gravitational scattering from high-order MMR as a dynamical cause to explain the observed orbital velocity dispersion for members of the Pasiphae family.

**Key words:** methods: *N*-body simulations – methods: numerical – celestial mechanics – planets and satellites: individual: Ananke – planets and satellites: individual: Himalia – planets and satellites: individual: Themisto.

## 1 INTRODUCTION

The existence of natural satellites in orbit around the giant planets of our Solar system has been known since Galileo discovered the four inner regular moons of Jupiter. Since then two classes of natural satellites have been identified to orbit the outer giant planets: regular and irregular satellites. The study of irregular satellites is interesting as they are located close to the Hill sphere boundary of the parent planet. Consequently, solar perturbations are present and chaotic behaviour is expected in the time evolution of their orbits. Recent

reviews on the subject of irregular satellites are given in Peale (1999) and Jewitt & Haghighipour (2007), Nicholson et al. (2008). Regular satellites are characterized by prograde circular orbits located close to the equatorial plane of the planet. This is the case of the Galilean satellites of Jupiter. The class of irregular satellites differs in being on large eccentric and highly inclined orbits in either prograde (direct) or retrograde motion.

The majority of the current population of giant planet irregular satellites have been discovered by ground-based large aperture optical telescopes operating in dedicated survey programs over the past 10 yr (Gladman et al. 1998, 2000, 2001; Sheppard & Jewitt 2003; Holman et al. 2004; Sheppard, Jewitt & Marsden 2005; Sheppard, Jewitt & Kleyna 2006). The most abundant irregular satellite

★E-mail: tobiash@astro.ku.dk

population is observed to exist at Jupiter counting approximately 60 members at the current time.

The regular Galilean satellites are thought to have formed by accretion processes within a circum-Jovian planetary disc (Canup & Ward 2002; Mosqueira & Estrada 2003; Estrada & Mosqueira 2006). Observed kinematic differences between regular and irregular satellite orbits suggest a different formation mechanism for irregular satellites. The most favoured formation scenario is captured from an initial heliocentric orbit. The key element of permanent capture is the necessity of a frictional force (due to a gaseous environment) or energy transfer during a close encounter. Both processes are capable of dissipating orbital energy and provide a viable dynamical route to form a given population of irregular satellites. For a description of various capture scenarios, we refer to Jewitt & Haghighipour (2007) and references therein.

Several authors have studied general stability properties of irregular satellites. Haghighipour & Jewitt (2008) studied the region between Callisto and the innermost Jovian irregular satellite Themisto ( $30R_{\text{Jup}} < r < 80R_{\text{Jup}}$  where  $R_{\text{Jup}}$  is Jupiter's radius, and  $r$  is the distance of the satellite to Jupiter). Despite observational evidence indicating that this region is devoid of satellites, they showed that a large fraction of this region allows stable satellite orbits for at least 10 Myr. Extensive stability surveys of irregular satellites within the Hill sphere of the giant planets have been carried out by Carruba et al. (2002) and Nesvorný et al. (2003) by recording the lifetimes of irregular satellite test particles in various parameter surveys. Yokoyama et al. (2003) studied the region  $250R_{\text{Jup}} < r < 370R_{\text{Jup}}$  for prograde Jovian irregular orbits in the semimajor axis and inclination plane finding evidence for the presence of secular resonances (Whipple & Shelus 1993; Ćuk & Burns 2004; Nesvorný & Beaugé 2007). Stability properties of irregular orbits at the outer regions of the giant planet's Hill sphere and beyond were studied by Shen & Tremaine (2008).

Motivated to study the phase-space topology structure of irregular satellites in detail, we applied the Mean Exponential Growth Factor of Nearby Orbits (MEGNO) chaos indicator (Cincotta & Simó 2000; Goździewski et al. 2001; Cincotta, Giordano & Simó 2003) to qualitatively differentiate between quasi-periodic and chaotic phase-space regions. Initial tests showed that MEGNO is efficient in showing chaotic regions using relative short integration times of the orbit. In this work, we outline the basic principles of the MEGNO indicator as this is the first time this technique is applied to the dynamics of irregular satellites.

An interesting dynamical property of the phase-space distribution of orbital elements is the clustering in distinct families for both prograde and retrograde irregular satellite members (Nesvorný et al. 2003; Nesvorný, Beaugé & Dones 2004). Assuming the observed satellite families have been formed by collisional fragmentation of two progenitor satellites, Nesvorný et al. (2003) identify a contradiction involving inconsistencies in the observed velocity dispersion of Jovian irregular satellites. While the excess in the velocity dispersion of the prograde Himalia group can be explained by gravitational scattering by the largest member (Christou 2005), an additional dynamical mechanism needs to be identified to explain the velocity dispersion of the retrograde families. To further disperse the velocity distribution of retrograde satellite families, we hypothesize gravitational scattering of the orbits of Pasiphae family members by high-order mean-motion resonances (MMRs) as a possible physical cause.

The structure of the paper is as follows. In section 2, we present the model and numerical methods used as well as initial conditions and definitions of angular variables. Section 3 presents a review of

the MEGNO chaos indicator and an outline of its computation while illustrating and reviewing its relation to the maximum Lyapunov characteristic number as computed from the classic methods. Tests on numerical accuracy of our integrations are presented. Section 4 describes the construction of dynamical maps of Jovian irregular satellites as studied in this work. Section 5 outlines and discusses essential steps to obtain the secular system of the time variation of a satellite's Keplerian elements using a time-averaged running window to smooth the orbital elements. Section 6 presents our results with comparison to the previous work addressing the stability of Jovian irregular satellites. Two examples of chaotic and quasi-periodic orbits are studied under scrutiny. In section 7, we provide a summary and conclude this work, while pointing out and addressing possible avenues along future research.

## 2 MODEL, NUMERICAL METHODS AND INITIAL CONDITIONS

The results obtained in this work are based on the elliptic restricted three-body problem. We integrate the system of equations of motion with  $\mathbf{r}_i$  and  $\mathbf{v}_i$  denoting the position and velocity vectors of the  $i$ th body, respectively (Morbidelli 2002),

$$\frac{d\mathbf{r}_i}{dt} = \mathbf{v}_i \quad (1)$$

$$\frac{d\mathbf{v}_i}{dt} = -\frac{k^2(m_0 + m_i)\mathbf{r}_i}{\|\mathbf{r}_i\|^3} + \sum_{j=1, j \neq i}^N k^2 m_j \left[ \frac{\mathbf{r}_{ij}}{\|\mathbf{r}_{ij}\|^3} - \frac{\mathbf{r}_j}{\|\mathbf{r}_j\|^3} \right]. \quad (2)$$

In this work, we consider  $N = 2$  in a Jovian centric reference frame with  $m_0$  denoting the mass of Jupiter and  $k^2$  denotes the Gauss gravitational constant. Furthermore, we define  $\mathbf{r}_{ij} = \mathbf{r}_j - \mathbf{r}_i$  as the vector pointing from  $m_i$  to  $m_j$ , with  $\|\mathbf{r}_i\|$  denoting the Euclidean distance of  $\mathbf{r}_i$ . The positions (relative to Jupiter) and masses of the satellite and the Sun are  $(\mathbf{r}_1, m_1)$  and  $(\mathbf{r}_2, m_2)$ , respectively. In this model, the irregular satellite is orbiting Jupiter and its orbit is subject to gravitational solar perturbations. In all integrations, we regard the satellite as a test particle of zero mass. Oblateness effects from Jupiter are not considered in this model and perturbations from other planets or satellites are omitted as well. We consider this simplified model for two reasons. First, the purpose of this paper is to demonstrate and apply the MEGNO chaos indicator to the dynamics of irregular satellites, and secondly we aim qualitatively to identify chaotic regions originating from Solar perturbations only. If we were to include oblateness and planetary perturbations, cause and effect would be difficult to isolate. In future work, we plan to include additional sources of perturbations.

The orbit of the satellite was obtained by the numerical integration of equation (2) using: (1) the 15th-order RADAU integration algorithm as implemented in the latest version of the MERCURY package (Chambers & Migliorini 1997; Chambers 1999) and (2) the Gragg-Bulirsch-Stoer (GBS) extrapolation algorithm (Hairer, Norsett & Wanner 1993) as implemented in the CS-MEGNO code (Goździewski et al. 2001). The RADAU integrations were used to study individual satellite orbits (Figs 14 and 16), and the GBS integrator was used for the generation of MEGNO maps of irregular satellite phase-space regions. Using two different numerical algorithms on the same initial condition provides an independent test of a calculated orbit. Initial conditions (geometric Cartesian elements relative to Jupiter's centre of mass) for the Sun and observed irregular

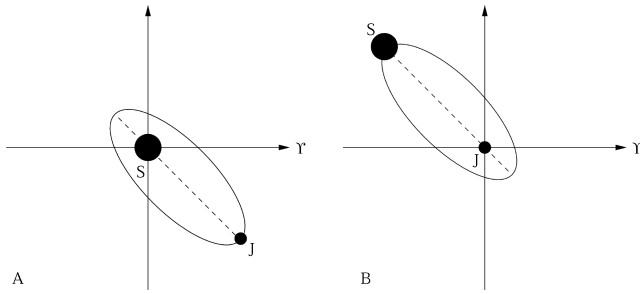


**Figure 1.** Graphical illustration of the relationship between angles in a heliocentric reference system and a planetocentric system. In both panels,  $\Upsilon$  denotes the reference direction from which inertial angles are measured and the orbital motion is counterclockwise. Panel A: shows the orbit of Jupiter (J) with respect to the Sun (S). Jupiter's orbit is strongly exaggerated in its eccentricity for reasons of clarity. In the current situation, the longitude of pericentre of Jupiter is  $\omega_J^{\text{hel}} = 135^\circ$ . Panel B: the orbit of Sun (S) with respect to Jupiter (J). Here, the longitude of perijove  $\omega_{\odot}^{\text{jov}} = 315^\circ$ .

satellites have been obtained from the JPL Horizon<sup>1</sup> Ephemeris generator (Giorgini et al. 1996) at the epoch 2005 January 01 (12:00UT). For the Sun only Cartesian vectors can be retrieved relative to Jupiter. For the computations of the stability maps (see Section 6.1), we have transformed the Sun's Cartesian elements to Keplerian elements using the `MCO_X2EL.F` subroutine as implemented in the latest version of `MERCURY`. The transformation introduces round-off absolute errors not larger than  $10^{-10}$  which is much smaller than the error in the observed elements of irregular satellites. The retrieved initial conditions are referred to the ecliptic and mean equinox (xy-plane is the orbit of the Earth) of the reference frame ICRF/J2000.0. In this work, we will present our results in a *planetocentric* reference system where Jupiter is at the centre and the ecliptic is the reference plane. Thus, we denote the planetocentric elements<sup>2</sup> of a satellite as  $(a, e, I, \omega, \Omega, M)$  (where  $M$  is the mean anomaly) and we use the subscript  $\odot$  to indicate the Sun's orbit relative to Jupiter and the subscript  $J$  to denote the orbit of Jupiter in the heliocentric reference system. For the longitude of perijove of prograde irregular satellites, we use the usual definition  $\varpi = \Omega + \omega$ . For retrograde satellites, we use  $\varpi = \Omega - \omega$ . The mean longitude of an irregular satellite is then given by  $\lambda = \varpi + M$ .

In order to compare our data with previous published results in the literature using both planetocentric and heliocentric orbital elements, we briefly point out the relationship of angles measured in the two reference frames. Changing the coordinate system from heliocentric to a Jovicentric system leaves the semimajor axis and eccentricity unchanged as these quantities are invariable under a coordinate transformation. In Fig. 1, we demonstrate the relationship between the longitude of pericentre of the two bodies in the two reference systems. If  $\omega_J^{\text{hel}}$  is the longitude of Jupiter in the heliocentric system and  $\omega_{\odot}^{\text{jov}}$  denotes the longitude of the Sun in the Jovicentric system, then from geometric arguments we have  $\omega_J^{\text{hel}} = \omega_{\odot}^{\text{jov}} + 180^\circ$ . A similar argument will lead to the relationship  $\lambda_J^{\text{hel}} = \lambda_{\odot}^{\text{jov}} + 180^\circ$  relating the mean longitudes of Jupiter and the Sun. The orbital inclinations ( $I_{\odot}, I_J$ ) and the arguments of node ( $\Omega_{\odot}, \Omega_J$ ) are unchanged under the transformation.

### 3 THE MEGNO CHAOS INDICATOR

The time evolution of irregular satellite orbits exhibits both quasi-periodic and chaotic dynamics (Saha & Tremaine 1993; Whipple & Shelus 1993; Goldreich & Rappaport 2003). An efficient numerical method to detect phase-space regions characterized by either chaotic or quasi-periodic initial conditions is provided by the MEGNO factor (or indicator). The MEGNO technique was first introduced by Cincotta & Simó (2000) and Cincotta et al. (2003) and was originally inspired from the concept of ‘conditional entropy of nearby orbits’ (CENO) (Cincotta & Simó 1999; Gurzadyan & Ruffini 2000). It can be applied to any dynamical system with more than two degrees of freedom and has found widespread applications in dynamical astronomy ranging from galactic dynamics to stability analysis of extrasolar planetary systems and Solar system small body dynamics (Goździewski et al. 2001; Goździewski, Bois & Maciejewski 2002; Goździewski 2002; Bois et al. 2003; Cincotta, Giordano & Simó 2003; Cincotta & Giordano 2004; Goździewski 2004; Breiter et al. 2005; Gayon & Bois 2008). Recent tests on MEGNO can be found in Frouard, Fouchard & Vienne (2008), Barrio, Borczyk & Breiter (2009) and Valk et al. (2009).

By numerically evaluating the MEGNO factor after a given integration time one obtains a quantitative measure of the degree of stochasticity of the system. One method (and references therein Morbidelli 2002; Dvorak, Freistetter & Kurths 2005) to discriminate between ordered (or regular) and chaotic satellite orbits, is the calculation of the system's Lyapunov characteristic exponents or Lyapunov characteristic numbers. Very often one is only interested in determining the maximum Lyapunov characteristic number. In this work, we will denote this number as MLN or  $\gamma_{\max}$ . From the definition, MEGNO is closely related to the maximum Lyapunov exponent (MLE) providing an alternative determination of this quantity.

In this work, we apply the MEGNO criterion to the dynamics of Jovian irregular satellites. Details on the MEGNO concept and its numerical computation can be found in Cincotta & Simó (2000), Cincotta et al. (2003) and Goździewski et al. (2001). Since the MEGNO technique is applied for the first time to the dynamics of irregular satellites, we give a short review of the most important aspects and properties of MEGNO and provide additional information on its numerical computation and application to irregular satellite orbits.

#### 3.1 The Lyapunov exponent

Studying a system of  $N$  gravitationally interacting masses, the system of the equations of motion as given by equation (2) can be written in compact notation as  $6N$  first-order differential equations,

$$\frac{dx}{dt} = f(x(t)), \quad \text{with } x \in \mathbb{R}^{6N}. \quad (3)$$

For a given trajectory of a satellite in phase space, the MLE ( $\gamma_{\max}$ ) provides a useful quantitative measure to study either its hyperbolic or quasi-periodic structure and is defined as (Morbidelli 2002; Cincotta et al. 2003)

$$\gamma := \lim_{t \rightarrow \infty} \frac{1}{t - t_0} \ln \left( \frac{\|\delta(t)\|}{\|\delta(t_0)\|} \right) = \lim_{t \rightarrow \infty} \frac{1}{t - t_0} \int_{t_0}^t \frac{\|\dot{\delta}(s)\|}{\|\delta(s)\|} ds, \quad (4)$$

where  $\delta(t) = [\delta r(t), \delta v(t)]$  is the variational vector, and  $\|\delta(t)\|$  measures the Euclidean distance in phase space between two initially nearby orbits as a function of time (note the difference in notation

<sup>1</sup> Telnet ssd.jpl.nasa.gov 6775.

<sup>2</sup> The orbital inclination of a satellite is measured relative to the ecliptic.

between  $\delta$  and  $\dot{\delta}$ ). The ratio  $\|\dot{\delta}\|/\|\delta\|$  measures the relative rate of change of the variational (separation) vector. The second equality in equation (4) is easily realized by the change of variables.<sup>3</sup>

The variational vector  $\delta(t)$  (or tangent vector or displacement vector) satisfies the linearized variational equations (Wisdom 1983; Morbidelli 2002; Cincotta et al. 2003; Skokos 2008),

$$\frac{d\delta(t)}{dt} = \dot{\delta}(t) = A(t)\delta(t), \quad (5)$$

where  $A$  is the Jacobian matrix with components  $A_{ij} = \partial f_i / \partial x_j$ .

For  $\gamma > 0$ , an initial separation grows exponentially in time (definition of chaotic motion) at the rate of  $e^{\gamma t}$  or decays, if  $\gamma < 0$ . In the case  $\gamma = 0$ , the time rate of change of the variational vector  $\dot{\delta}$  is zero with  $A$  vanishing indicating quasi-periodic or regular motion. Since the (elliptic) restricted three-body problem is a conservative system, the case  $\gamma < 0$  is never encountered and would indicate the presence of dissipative forces. In practical computations, the limit  $t \rightarrow \infty$  is physically (or computationally) not feasible and only a finite time estimate  $\gamma(T_{\max})$  of  $\gamma$  is obtained after integration time  $T_{\max}$ . We will denote this estimate as  $\gamma_{\max}$ . In finite-precision computations, the maximum representation of a real number is limited by the word length. To prevent a numerical overflow, the variational vector has to be renormalized in case of chaotic dynamics. In this work, we will pay some attention on the renormalization time. For classic computations of the MLEs, we refer to Benettin et al. (1980), Wisdom (1983) and Wolf et al. (1985). Recently Skokos (2008) provides a review on the computation of the Lyapunov characteristic exponents.

### 3.2 Asymptotic properties of MEGNO

The MEGNO indicator is closely related to the definition of  $\gamma$  and is defined as (Cincotta & Simó 2000; Cincotta et al. 2003)

$$Y(t) = \frac{2}{t} \int_{t_0}^t \frac{\|\dot{\delta}(s)\|}{\|\delta(s)\|} s \, ds, \quad (6)$$

along with its time-averaged mean value

$$\langle Y \rangle(t) = \frac{1}{t} \int_{t_0}^t Y(s) \, ds. \quad (7)$$

In the definition of  $Y$  the relative rate of change of the separation vector  $\dot{\delta}/\delta$ , is weighted with time during the integration giving preference to the memory of late evolutionary behaviour of the separation vector (Morbidelli 2002). The time-weighting factor introduces an amplification of any stochastic behaviour allowing the detection of hyperbolic regions in the time interval  $(t_0, t)$ . In addition, the MEGNO is computed based on the whole time interval in a given finite numerical integration. This property differentiates MEGNO from other chaos/quasi-periodicity indicators known in the literature as Fast Lyapunov Indicator (FLI), Smaller Alignment Index (SALI), Relative Lyapunov Indicator (RLI), Generalized Alignment Index (GALI) and the Frequency Map Analysis (FMA) technique (Laskar 1990; Froeschlé, Lega & Gonczi 1997; Skokos et al. 2003; Sándor et al. 2004; Skokos, Bountis & Antonopoulos 2007). Most of these methods differentiate between chaotic and quasi-periodic dynamics based on the current state of the system's variational vector. In this work, we do not intend to present a comparison study between various chaos/quasi-periodic detection techniques.

<sup>3</sup> If  $y = \delta(s)$ , then  $\int_{t_0}^t [\dot{\delta}(s)/\delta s] ds = \int_{t_0}^t (1/y) dy = \ln[y(t)/y(t_0)]$ .

### 3.2.1 Properties of $Y$ , $\langle Y \rangle$ for the quasi-periodic case

A property of MEGNO that makes its use interesting is the information content in  $\langle Y \rangle$  to distinguish between chaotic and quasi-periodic trajectories in phase space through a single quantity. In general,  $\langle Y \rangle$  can be parametrized as a linear function  $\langle Y \rangle(t) = \alpha t + \beta$ . In the case of regular quasi-periodic dynamics  $\alpha \sim 0$ ,  $\beta \sim 2$ . Furthermore following Cincotta & Simó (2000) and Cincotta et al. (2003), if the motion is quasi-periodic then  $Y$  will exhibit oscillations about 2 with  $\langle Y \rangle \rightarrow 2.0$  for  $t \rightarrow \infty$ .

Comparing the convergence rates in the case of regular quasi-periodic dynamics Cincotta et al. (2003) showed that in the limit  $t \rightarrow \infty$  the quantity  $\langle Y \rangle(t)$  converges faster towards zero when compared to the convergence rate of  $\gamma$ . In particular, from the theory  $\gamma$  asymptotically approaches zero as  $\ln(t)/t$  while  $\langle Y \rangle/t$  asymptotically approaches zero as  $2/t$ . We will demonstrate this property in a numerical example later in this work [e.g. Fig. 2(C)].

### 3.2.2 Properties of $Y$ , $\langle Y \rangle$ for the chaotic case

In the case of an chaotic orbit, the two quantities  $Y$  and  $\langle Y \rangle$  increase linearly in time. The rate of change for  $Y$  and  $\langle Y \rangle$  is approximately  $\gamma$  and  $\gamma/2$ , respectively. Specifically for  $\langle Y \rangle$ , we have  $\langle Y \rangle(t) = \alpha t + \beta$  with  $\alpha \sim \gamma/2$  and  $\beta \sim 0$ . Hence, the difference in the slopes implies that from the time after which an orbit exhibits chaotic behaviour  $\langle Y \rangle$  will be smaller than  $Y$ . It is important to note that in the case of ‘sticky’ orbits, the dynamics could initially exhibit quasi-periodic behaviour followed by a sudden transition to a chaotic behaviour (Sussman & Wisdom 1988; Milani & Nobili 1992; Milani, Nobili & Knezevic 1997).

Furthermore, we have  $\langle Y \rangle(t) = \gamma t/2$  for  $t \rightarrow \infty$ . The latter equation relates the Lyapunov characteristic number to the limiting value of  $\langle Y \rangle(t)$  at integration time  $t$ . In particular, the quantity  $2\langle Y \rangle/t$  would provide an alternative estimation of the maximum Lyapunov characteristic number  $\gamma$  in a  $[\log(\gamma), \log(t)]$  diagram. However, taking advantage of the smooth property of  $\langle Y \rangle$  as a consequence of the averaging, a linear least squares fit to this quantity would recover the Lyapunov characteristic number (Cincotta & Simó 2000; Goździewski et al. 2001; Cincotta et al. 2003). Later in this work, we will demonstrate these properties of  $Y$  and  $\langle Y \rangle$  in some more detail for quasi-periodic and chaotic orbits of two hypothetical Jovian irregular satellites (cf. Section 3.7).

### 3.3 Numerical calculation of $Y(t)$ and $\langle Y \rangle(t)$

In practice,  $Y(t)$  and  $\langle Y \rangle(t)$  are calculated by rewriting equations (6) and (7) into two differential equations (Goździewski et al. 2001),

$$\frac{dx}{dt} = \frac{\dot{\delta} \cdot \delta}{\|\delta\|^2} t \quad \text{and} \quad \frac{dw}{dt} = 2\frac{x}{t}, \quad (8)$$

To obtain  $x(t)$ ,  $w(t)$  the two first-order coupled differential equations are solved numerically (ODEX algorithm) in parallel with the equations of motion. Then,  $Y(t)$  and  $\langle Y \rangle(t)$  can be determined from  $Y(t) = 2x(t)/t$  and  $\langle Y \rangle(t) = w(t)/t$  at the end of each integration step.

### 3.4 The classic $N$ -body variational equations

The variational vector  $\delta = (\delta r_i, \delta v_i)$  and its time derivative  $\dot{\delta} = (\delta \dot{r}_i, \delta \dot{v}_i)$  of the  $i$ th body are obtained by solving the variational equations of motion (again, note the difference between  $\delta$  and  $\dot{\delta}$ ). In parallel with the Newtonian equations of motion, we have for

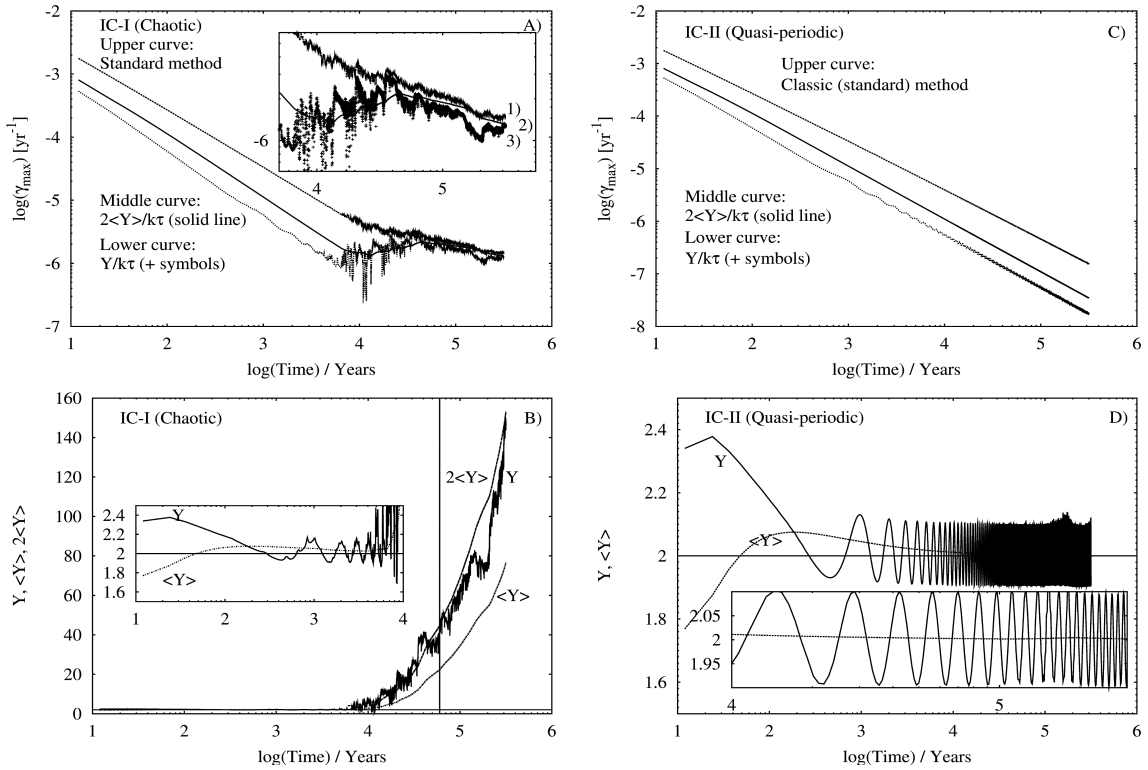


**Figure 2.** Comparing MEGNO with the classic (or standard) computation of the MLE ( $\gamma_{\max}$ ) for two different orbits IC-I (panels A and B) and IC-II (panels C and D). For details on initial conditions see Table 1 and Fig. 9. For both cases, we renormalized the displacement vector every orbital period of Jupiter (or Sun in this work). Panel A: three curves are shown. The upper curve is  $\gamma_{\max}$  as calculated using the classic method. This curve ends at (1) in the inset figure. The middle curve is  $2\langle Y \rangle / k\tau$  smooth because of the averaging and ends at (2). The lower curve is  $Y/k\tau$ . Note that during the quasi-periodic phase the rate of change of  $Y$  and  $\langle Y \rangle$  is different as expected from the theory. When the orbit becomes chaotic the rate of change of  $Y$  and  $2\langle Y \rangle$  is the same (the MLE) and coincides with the MLE as calculated from the standard method. Panel B: here, we show the corresponding time evolution of  $Y$ ,  $\langle Y \rangle$  and  $2\langle Y \rangle$  with all three quantities evolving in time as expected from the theory. See text for details. Note the logarithmic scale on the time axis disguising the linear character of  $Y$ ,  $\langle Y \rangle$ . The vertical line corresponds to the chosen maximum integration time to generate our MEGNO maps. Panel C: here, no flattening of all three curves towards a non-zero  $\gamma$  is observed as is expected for regular motion during the course of the 60 000 yr integration. The two lower (MEGNO) curves converge faster towards zero when compared to the top-most curve. Panel D: time evolution of  $Y$ ,  $\langle Y \rangle$  as expected from the theory. See text for more details.

the  $i$ th body the following equations of motion for the displacement vector (or the variational equations)<sup>4</sup> in velocity and acceleration and given by (Mikkola & Innanen 1999)

$$\frac{d\delta\mathbf{r}_i}{dt} = \delta\mathbf{v}_i, \quad (9)$$

$$\frac{d\delta\mathbf{v}_i}{dt} = -k^2(m_0 + m_i) \left( \frac{\delta\mathbf{r}_i}{\|\mathbf{r}_i\|^3} - \frac{3\mathbf{r}_i(\mathbf{r}_i \cdot \delta\mathbf{r}_i)}{\|\mathbf{r}_i\|^5} \right) - \delta\mathbf{A}_i, \quad (10)$$

the first two terms describe the variation in the 2-body Kepler orbit and the variation in perturbations (or interactions) is

$$\delta\mathbf{A}_i = - \sum_{j=1, j \neq i}^N m_j \left\{ \left[ \frac{\delta\mathbf{r}_{ij}}{\|\mathbf{r}_{ij}\|^3} - \frac{3\mathbf{r}_{ij}(\mathbf{r}_{ij} \cdot \delta\mathbf{r}_{ij})}{\|\mathbf{r}_{ij}\|^5} \right] \right. \quad (11)$$

$$\left. - \left[ \frac{\delta\mathbf{r}_{0j}}{\|\mathbf{r}_{0j}\|^3} - \frac{3\mathbf{r}_{0j}(\mathbf{r}_{0j} \cdot \delta\mathbf{r}_{0j})}{\|\mathbf{r}_{0j}\|^5} \right] \right\}, \quad (12)$$

where  $\mathbf{r}_{ij} = \mathbf{r}_j - \mathbf{r}_i$ ,  $\delta\mathbf{r}_{ij} = \delta\mathbf{r}_j - \delta\mathbf{r}_i$ ,  $\delta\mathbf{r}_{0j} = \delta\mathbf{r}_j - \delta\mathbf{r}_0$  and the zero superscript denotes the central body. In this work, we have  $N = 2$  (irregular satellite and the Sun). Equations (9) and

<sup>4</sup> Obtained from total differentiation of the Newtonian equations of motion and we note that  $\delta\mathbf{r}_i = \mathbf{r}_i \delta\mathbf{r}_i / r_i$ .

(10) are computed in a straightforward way once the initial conditions have been defined for initial Kepler orbit ( $\mathbf{r}$ ,  $\mathbf{v}$ ) and the initial displacement vector (variational) ( $\delta\mathbf{r}$ ,  $\delta\mathbf{v}$ ) for each body. Initial condition for the variational displacement vector is chosen using the random generator RAN0.F from Press et al. (1996) with  $\|\delta_0\| = 1$ .

### 3.5 Classic computation of MLE ( $\gamma_{\max}$ )

The classic computation of the MLE including renormalization has been introduced by Benettin, Galgani & Strelcyn (1976) and Benettin et al. (1980). If  $\tau$  denotes the renormalization time then the MLE can be computed from Tancredi & Sánchez (2001), Morbidelli (2002) and Skokos (2008),

$$\gamma = \lim_{k \rightarrow +\infty} \frac{1}{k\tau} \sum_{i=1}^k \ln \frac{\|\delta(k\tau)\|}{\|\delta_0(k\tau)\|}, \quad (13)$$

where  $\delta$  is the variational vector (as defined previously) and in practice the limit  $k \rightarrow k_{\max}$  is evaluated with  $k_{\max}$  some finite step number. Ferraz-Mello (1994) refers to the above recipe as the rescaling procedure of Benettin et al. (1976). For initial conditions located in hyperbolic phase-space domains, the magnitude  $\|\delta\|$  might lead to numerical overflow during the numerical computation on a precision-limited computer. This is because of the

character of exponential divergence of the time evolution of  $\delta$  in chaotic regions of phase space. Therefore, the variational vector has to be renormalized at fixed intervals of time to avoid numerical overflow. For chaotic dynamics, the above procedure will yield the MLE ( $\gamma_{\max}$ ) as a limiting non-zero (and positive) value for sufficiently long integration times. The corresponding Lyapunov time is defined as  $1/\gamma_{\max}$  and denotes the onset time of chaotic behaviour at which the displacement vector has increased by  $e \sim 2.718$ . To compute  $\gamma_{\max}$  from equation (13), we implemented the algorithm as outlined in Skokos (2008, p. 34). At each renormalization time the variational displacement is normalized ensuring the preservation of the original orientation at that time (i.e. initially and at each step  $k$  we have  $\|\delta_0\| = 1$ ). The displacement vector is obtained from solving the linearized variational equations of motion. This is the classic or standard computation of  $\gamma_{\max}$  and will be used to compare with the MEGNO estimate of  $\gamma_{\max}$ . This provides an opportunity to compare the two methods with each other for a numerical estimate of  $\gamma_{\max}$ . At this point, it is important to highlight that both methods are based on the same variational approach (as opposed to the less reliable two-particle shadow technique) as recommended by Tancredi & Sánchez (2001). However, the computation of  $\gamma_{\max}$  from each method is fundamentally different. Finally, in real numerical computations there is no a priori knowledge on the proper choice of the renormalization period and the length of integration as these depend on the dynamical system under study. However, in a later discussion, we provide tests and argue that the final estimate of  $\gamma_{\max}$  is independent of the renormalization period for a particular chaotic orbit.

### 3.6 Computing $\gamma_{\max}$ from two different methods

In the following we compare the computation of the maximum Lyapunov characteristic number from two distinct methods given by the direct classic (or standard) method (equation 13) and as determined from the MEGNO theory. We will consider the computation of the maximum Lyapunov number in a classic log  $\gamma(t)$  versus  $\log t$  graph. For completeness, we study the case of a chaotic and quasi-periodic orbit. Both orbits are integrated for  $\sim 300\,000$  yr. For details on initial conditions, we refer to Fig. 9. In Fig. 2(A), we show the time evolution of equation (13),  $2\langle Y \rangle/k\tau$  and  $Y/k\tau$  since the orbit becomes chaotic after an initial transient period of quasi-periodicity (from 0 to 6000 yr). For a chaotic orbit  $Y$  and  $2\langle Y \rangle$  increase at the same rate and both quantities will be on the same order of magnitude at a given time. While  $Y$  exhibits oscillations, the evolution of  $\langle Y \rangle$  is more smooth (middle curve, solid line). At the end of the integration, all three values converge to the maximum Lyapunov characteristic number  $\gamma_{\max} = 1.5 \times 10^{-6}$  corresponding to a Lyapunov time of 666 667 yr.

In Fig. 2(C), we show a similar calculation for a quasi-periodic orbit. As expected, the linear curves do not flatten within the integration time. The top-most curve corresponds to the classic computation, while the middle and lower curves are obtained from MEGNO. We chose to plot  $Y$  and  $2\langle Y \rangle$  to highlight the oscillating terms in  $Y$ . Finally, while initially the MEGNO computation of  $\gamma$  converges faster towards zero the two methods have similar convergence rates at larger times. We conclude that both independent numerical approaches result in a consistent value of  $\gamma_{\max}$ .

### 3.7 Detailed properties of $Y$ and $\langle Y \rangle$

In the following, we provide examples and illustrate several properties of the time evolution of  $Y$  and  $\langle Y \rangle$  for regular and chaotic

motion. For a quasi-periodic orbit, Cincotta et al. (2003) showed in general that  $Y$  oscillates around  $Y = 2$  with bounded amplitude studying quasi-periodic orbits. From the theory, the peaks of oscillations have the same amplitudes, and from the definition of the average  $\langle Y \rangle$  (equation 7) it has been shown that  $\langle Y \rangle \rightarrow 2$ . 0 for  $t \rightarrow \infty$  while the amplitude of  $\langle Y \rangle$  decreases as  $\sim 1/t$  asymptotically (Cincotta et al. 2003). In this work, we confirm this behaviour when applied to the dynamics of irregular satellites. An example of this prediction from the theory is shown in Fig. 2(D) demonstrating the time evolution of  $Y$ ,  $\langle Y \rangle$  for a quasi-periodic orbit (IC-II). We observe oscillations of constant amplitude of  $Y$  and note the asymptotic behaviour of  $\langle Y \rangle$  (see small inset figure). Note the short burst of  $Y$  between  $10^5$  and  $2 \times 10^5$  yr. This modulation in amplitude might be explained by the close proximity of this orbit to the global hyperbolic region (Cincotta et al. 2003 calls this the large chaotic sea when considering the Hénon-Heiles system) in phase space as shown in Fig. 9 or due to the close proximity of the chaotic 5:1 MMR.

Moreover, from the theory in the case of a chaotic orbit both  $Y$  and  $\langle Y \rangle$  grow linearly with time with  $Y$  given by (p. 155 Cincotta et al. 2003)

$$Y(t) = \gamma_{\max}t + \mathcal{O}(t). \quad (14)$$

Here, the growth rate is equal to the MLE and  $\mathcal{O}(t)$  denoting additional time depending oscillating terms with zero average. Following Cincotta et al. (2003) after averaging and considering the limit  $t \rightarrow \infty$ , we have  $\langle Y \rangle$  given by

$$\langle Y \rangle(t) = \frac{1}{2}\gamma_{\max}t. \quad (15)$$

Therefore, in the case of probing a chaotic orbit in phase space the growth rate of  $\langle Y \rangle$  is half the growth rate of  $Y$ . Hence, in a  $\langle Y \rangle$ ,  $Y$  versus  $t$  plot the quantity  $\langle Y \rangle$  will always be lower than  $Y$ . We show this in Fig. 2. In principle when comparing the two quantities,  $Y$  should be compared with  $2\langle Y \rangle$  when aiming to demonstrate that both quantities grow at the same constant time-rate as given by equations (14) and (15). Fig. 2(B) shows the time evolution of  $Y$ ,  $\langle Y \rangle$ ,  $2\langle Y \rangle$  for a chaotic orbit (IC-I). For the first 5000 yr (see small inset figure), the system appears to evolve quasi-periodic. As discussed earlier during this time,  $Y$  oscillates with a constant amplitude around 2 with  $\langle Y \rangle$  decreasing asymptotically and approaching 2. From 6000 yr and onwards  $Y$  starts to grow at a constant rate clearly indicating that this initial condition was started in a hyperbolic region of phase space. In this case, the physical cause of chaos is the nearby 5:1 MMR (cf. Fig. 9). In principle, in the chaotic case a numerical estimate of the MLE can be determined from a least-squares fit to the time evolution of  $\langle Y \rangle$ . To show that  $Y$  and  $\langle Y \rangle$  grow at the same rate, we have also plotted  $2\langle Y \rangle$  in the same figure panel from 6000 yr and onwards. We conclude this section to have numerically recovered basic properties of MEGNO as predicted from the theory when applied to the dynamics of irregular satellites.

### 3.8 Test: renormalization time

We have investigated the effect/dependency of the renormalization time on the final value of  $\gamma$  for the classic and MEGNO methods. Integrating the equations of motion (and variational equations) over subintervals of 12 yr, we have considered five renormalization times.  $\tau = 1, 10, 100$  and  $500 P_\odot$ . We show our results in Fig. 3 and observe that the final value of  $\gamma_{\max}$  is independent from  $\tau$ . We chose to output data with a frequency equivalent to the renormalization time in a given run. Data are therefore available after  $\tau$  years with

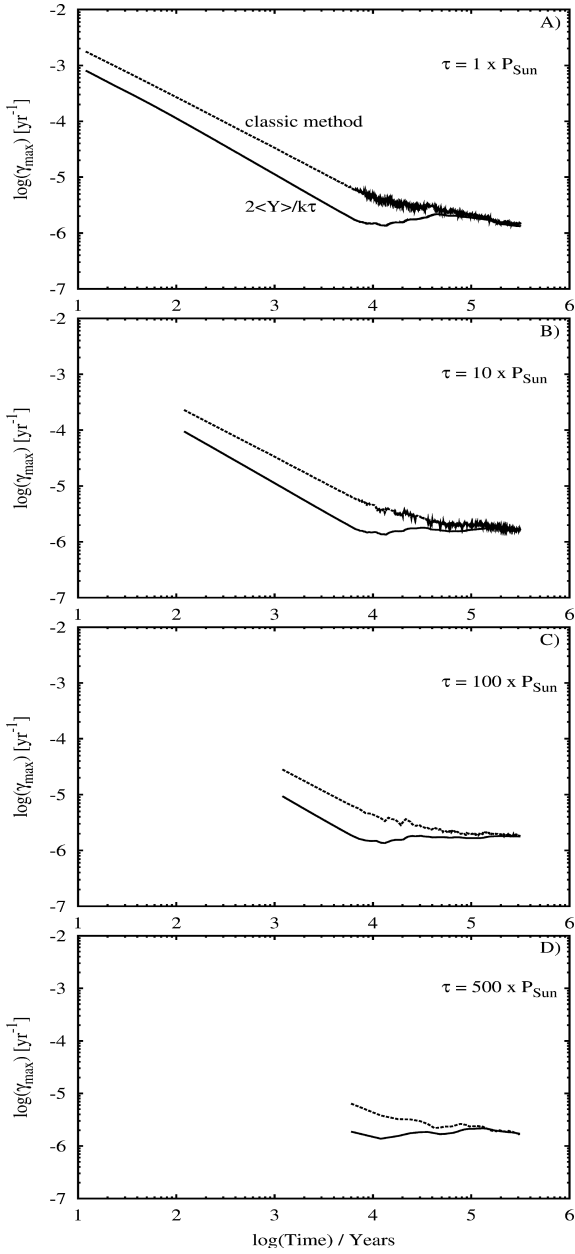


**Figure 3.** Computing the maximum Lyapunov characteristic number for initial condition IC-I considering different renormalization times,  $\tau$ . The partition time-step for integration is set to 12 yr (orbital period of Jupiter) with the maximum number of steps in the GBS algorithm set to 10 000. It is evident that the final Lyapunov time is independent of the renormalization time. See text for more details.

the number of data decreases as  $\tau$  increases. In Fig. 3(A), data are available every 12 yr, while for Fig. 3(D) data are available every 6000 yr. This explains the sparsely sampling of  $\gamma$  in Figs 3(B)–(D). It is important to note that the difference (if any) between panel A and D is due to the renormalization time and not the sampling frequency at which  $\gamma$  is measured. In all four tests, the same initial condition and an identical numerical integration of the orbit and the displacement vector were used. We conclude this section by stating that the rescaling procedure has no effect on the computation of the maximum Lyapunov characteristic number. In this work, we renormalize the variational displacement vector every orbital period

of the Sun (Jupiter) to ensure no numerical overflow when probing chaotic regions of phase space.

### 3.9 Numerical integration and accuracy tests

The MEGNO indicator is numerically computed as outlined in the previous section using the Gragg-Bulirsch-Stoer (GBS) integration algorithm (Hairer et al. 1993). All computations are carried out using double precision arithmetic. To control the numerical errors during computations two accuracy parameters are necessary for a GBS integration. The two parameters control the absolute ( $\delta$ , not to confuse with the variational symbol) and relative ( $\epsilon$ ) error tolerances for any given integration and both need to be specified for a given accuracy requirement.

When integrating the equations of motion (and variational equations) from time  $t_0$  to some time  $T_{\max}$  in the future, we partition this interval into subintervals and iteratively integrate the system for a number of cycles  $k$ . For a given accuracy requirement, the explicit GBS algorithm needs a minimum number of steps (controlled by the Maximum Number of Steps (NMAX) parameter) to successfully determine the system's state at the end point of a given subinterval. If the number of steps chosen is too small, the algorithm will fail to reach the end point of a given subinterval. When applied to orbital dynamics this is important to note in the event of close approaches or perijove passages of moderate to high eccentric satellite orbits. In the case, where the partition time length of a given subinterval chosen is too large and the number of steps is too small, the algorithm is likely to fail or providing less accurate results. Using the default setting of the NMAX parameter (10 000) in the GBS ODEX.F routine the above numerical pitfalls can be avoided by choosing a small subinterval. For a given choice in the maximum number of steps, the maximum subinterval needs to be determined from numerical experiments. In this work, this time interval is chosen to be equivalent to the orbital period of the Sun (or Jupiter) allowing a maximum of 10 000 steps for the completion. Integrating 60 000 yr would then require 5000 cycles each lasting for 12 yr.

In practical computations, the usual choice of  $(\delta, \epsilon)$  falls into the range from one part in  $10^9$  down to the limit of the machine precision ( $10^{-16}$ ) (depending on architecture). To find a suitable  $(\delta, \epsilon)$  set, we integrated several two-body Kepler problems for 10 Myr by following the two-body orbit of Himalia. In that case, the motion is expected to be a quasi-periodic (being more precise the orbit is periodic), and we use it as a test case to determine confidence of the computed MEGNO indicator which should converge to  $\langle Y(t) \rangle = 2.0$ . Initial numerical tests showed that the convergence of  $\langle Y \rangle$  depends on the accuracy of the numerical integration. This property was already outlined in Goździewski et al. (2001). We integrated Himalia's orbit (without Solar perturbations) for different combinations of the tolerance parameters. In total, we considered  $(14 \times 14)$  combinations with  $(\delta, \epsilon)$  ranging from  $10^{-10}$  to  $10^{-16}$ . The result of the integrations is shown in Fig. 4. The left-figure panel shows the numerical value of  $\langle Y \rangle$  (grey-scale colour coded) at the end of the integration for a given combination of  $(\delta, \epsilon)$ . The right-hand panel in Fig. 4 shows the time evolution of  $\langle Y(t) \rangle$  of a few selected combinations of the tolerance parameters. The  $(\delta, \epsilon)$  combinations resulting in the cases denoted by (A)–(E) are evidently of poor numerical accuracy showing  $\langle Y \rangle \gg 2.0$  after 10 Myr. We interpret this result as artificial numerical chaos, the result of the poor resolution of time discretization in the integration algorithm. The cases (F)–(I) show a significant better agreement with the expected value of  $\langle Y \rangle = 2.0$  with some numerical fluctuation of  $\langle Y \rangle$  observed during the integration. From the numerical experiments, we fix

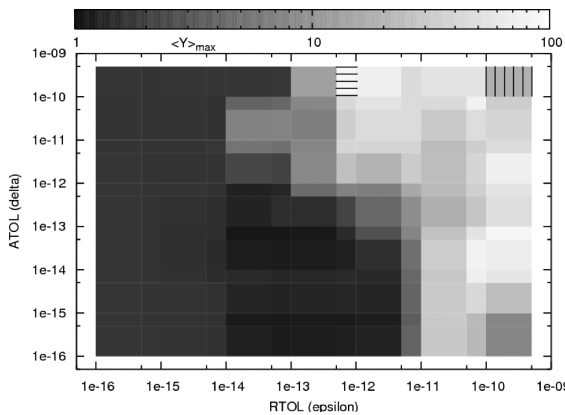


**Figure 4.** Results from two-body Kepler integrations. Right-hand panel: (A) (RTOL, ATOL) =  $(5.0 \times 10^{-11}, 1.0 \times 10^{-10})$ ; (B) (RTOL, ATOL) =  $(5.0 \times 10^{-13}, 1.0 \times 10^{-10})$ ; (C) (RTOL, ATOL) =  $(1.0 \times 10^{-11}, 1.0 \times 10^{-11})$ ; (D) (RTOL, ATOL) =  $(1.0 \times 10^{-12}, 1.0 \times 10^{-13})$ ; (E) (RTOL, ATOL) =  $(5.0 \times 10^{-12}, 1.0 \times 10^{-13})$ ; (F) (RTOL, ATOL) =  $(1.0 \times 10^{-16}, 1.0 \times 10^{-16})$ ; (G) (RTOL, ATOL) =  $(1.0 \times 10^{-15}, 1.0 \times 10^{-15})$ ; (H) (RTOL, ATOL) =  $(1.0 \times 10^{-14}, 1.0 \times 10^{-10})$  and (I) (RTOL, ATOL) =  $(5.0 \times 10^{-15}, 1.0 \times 10^{-12})$ . The area marked with vertical lines corresponds to case (D) and horizontal line corresponds to case (B). The final value after 10 Myr of  $\langle Y \rangle$  for case (F) was 1.999 757, case (G) 2.000 367, case (H) 1.636 787 and case (I) 1.798 234.

$(\delta, \epsilon) = (10^{-16}, 10^{-15})$  for all MEGNO computations in the present work. In addition, we monitor the relative energy error  $dE/E$  and note the maximum value reached during a given integration. For our choice of the tolerance parameters the average maximum relative energy error is on the order of  $dE/E \sim 10^{-11}$  over 1 Myr. We monitored and examined the relative energy error of several test orbits and found the time evolution to exhibit random walks with no systematic trends. For all orbits, the maximum relative energy error was smaller than  $10^{-12}$ , though in the restricted three-body problem this does not reflect the accuracy of the orbit of a massless test satellite. For that reason, we follow the same approach as outlined in Nesvorný et al. (2003) and monitored the Jacobi constant during the numerical integration (with the Sun on a circular orbit) and found a maximum relative change of this quantity to be on the order of typically  $10^{-5}$ . We also computed the absolute error of the semimajor axis ( $\|a_{\odot}(t) - a_{\odot}(t_0)\|$ ) of the Sun and found it to be less than a few parts in  $10^{-12}$ . This means a preservation of eight significant digits of the Sun's semimajor axis over 60 000 yr. Hence, no secular giant planet perturbations in the orbit of a satellite are present. Since we are not aiming at generating high-accuracy ephemerides of irregular satellite orbits, we consider these tests as sufficiently reliable in order to establish confidence in our results presented in this work. In addition, uncertainties in observed orbital elements of irregular satellites are assumed to be much greater than rounding/truncation errors introduced by the numerical integration algorithm. As a final test, we have also computed MEGNO by retaining only the components of the variational vector  $\delta$  for the satellite and compared the results with  $\delta$  for the whole system. As the orbit of the Sun represents a Kepler orbit, we conclude that any deviation of  $\langle Y \rangle$  from 2 is solely associated with the chaotic character of the test satellite orbit.

### 3.10 Numerical examples of test orbits and limitations

As an example, Fig. 5 shows the time evolution of  $Y(t)$ ,  $\langle Y \rangle(t)$  for the irregular satellite Ananke over a time-span of 1 Myr. We chose to plot  $Y$ ,  $\langle Y \rangle$  as a function of time and note that the time rate of  $\langle Y \rangle$  is smaller than the time rate of  $Y$ . In this numerical integration, only gravitational perturbations from the Sun were included. Initial conditions were retrieved from JPL Horizons Ephemeris with  $a_0 \sim 0.145$  au,  $e_0 \sim 0.38$ ,  $I_0 \sim 152^\circ$ . From Fig. 9, it is evident that this

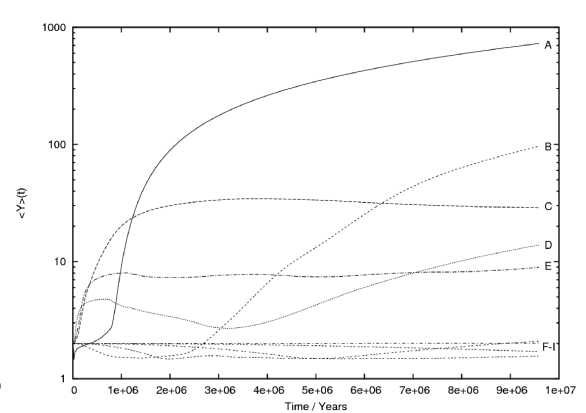


**Figure 5.** Time evolution of  $Y(t)$ ,  $\langle Y \rangle(t)$  and  $2\langle Y \rangle(t)$  from a numerical integration over 1 Myr for the retrograde satellite Ananke including only solar perturbations. The solid horizontal line indicates  $\langle Y \rangle = 2.0$ .

orbit is started close to chaotic structures (MMR) in phase space. We observe that Ananke's orbit exhibits a weak sign of chaotic behaviour as it is evident that no clear convergence of  $\langle Y \rangle \rightarrow 2$  is observed. The regular peaks in  $Y$  might be explained if this orbit frequently encounters a hyperbolic structure (possibly weak MMR) in phase space (see discussion in Cincotta et al. 2003 for an analogue behaviour in the Hénon-Heiles system).

In Fig. 6, we show the results of calculating  $\langle Y \rangle$  of four selected irregular satellites (Carme, Himalia, Sinope and Themisto) over 1 Myr. Our results suggest that both Themisto and Himalia (both on prograde orbits) show chaotic behaviour as their calculated  $\langle Y \rangle$  shows clear sign of divergence from 2.0. The contrary is seen for the orbits of Carme and Sinope (both on retrograde orbits) indicating convergence towards 2.0 indicating quasi-periodic time evolution. This result is in agreement with what is expected from numerical simulations. Prograde orbits tend to be less stable compared to retrograde orbits (Hamilton & Krivov 1997; Nesvorný et al. 2003). On comparison, the orbit of Carme and Sinope is displaced away from the presence of MMR (cf. Fig. 9) when compared to Ananke's orbit. This might explain the lack of chaotic behaviour for Carme and Sinope as observed in Fig. 6. It is noteworthy that although the calculation of  $\langle Y \rangle$  is a powerful numerical tool for the detection of chaotic phase-space regions it is necessary to be cautious when

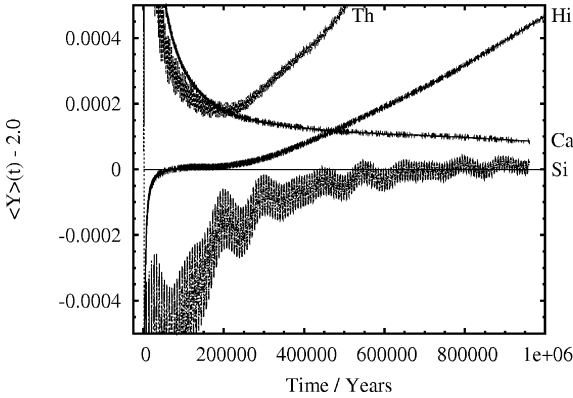


**Figure 6.** Time evolution of  $\langle Y \rangle$  for different selected irregular satellites over a time-scale of 1 Myr. The shown satellites are Th(emisto), Hi(malia), Ca(rme) and Si(nope).

interpreting results. As mentioned previously two of the irregular satellites (Themisto and Himalia) show a weak sign of chaotic behaviour with  $\langle Y \rangle$  diverging from 2.0 with  $|\langle Y \rangle - 2.0| < 0.0003$  after 200 000 yr. In a MEGNO map (see Fig. 9), such an initial condition would appear as quasi-periodic considering the large range when colour coding  $\langle Y \rangle$  for a given phase-space plane. Therefore, it is imperative to point out that every numerical tool used to differentiate between quasi-periodic and chaotic behaviour is only capable of showing quasi-periodicity up to the integration time. The apparent quasi-periodic orbit might subsequently change its dynamical character into a chaotic orbit. This behaviour was observed for the orbit of Pluto when considering long enough times (Sussman & Wisdom 1988). On the contrary once chaotic behaviour (excluding numerical chaos) has been detected, the orbit can be claimed chaotic for all times. If each initial condition in the MEGNO maps for irregular satellites presented in this work was calculated on time-scales similar to the age of the Solar system, it is likely that no quasi-periodic orbits would be detected. We will demonstrate later that an advantage of applying the MEGNO technique to the dynamics of irregular satellites is the identification of high- and low-order MMR as well as additional hyperbolic phase-space structures that lead to chaos. In our MEGNO maps, we can, with high confidence, associate chaotic regions with unstable orbits where the satellite either escapes or experiences a collision with one of the inner moons or if the eccentricity grows high enough (due to the Kozai mechanism) the satellite may even collide with Jupiter itself.

#### 4 CONSTRUCTION OF MEGNO, MS AND ME MAPS

In this work, we colour code the MEGNO indicator on a two-dimensional phase-space section mapping out the dynamics of irregular satellites. In particular, we show the dynamics in  $(a, I)$ -space, where  $a$  is the semimajor axis and  $I$  denotes the orbit inclination. We chose initial conditions in which orbit inclinations are relative to the ecliptic (see section on initial conditions). For a given range in semimajor axis and inclination, the grid of initial conditions in the maps is given by

$$a_i = a_{\min} + \frac{\Delta a}{N_x} i = a_{\min} + \frac{a_{\max} - a_{\min}}{N_x} i, \quad (16)$$

and

$$I_j = I_{\min} + \frac{\Delta I}{N_y} j = I_{\min} + \frac{I_{\max} - I_{\min}}{N_y} j, \quad (17)$$

where  $i = 0, \dots, N_x$  and  $j = 0, \dots, N_y$  are integers defining the grid resolution. Choosing a large  $(N_x, N_y)$  will result in a more detailed mapping of phase-space structures in  $(a, I)$  space. The range in semimajor axis is chosen to span  $a \in [0.04, 0.20]$  au ( $[0.11, 0.56] R_H$ ,  $[83, 419] R_{Jup}$ ). Satellite inclinations cover the range  $I \in [0^\circ, 180^\circ]$  considering both prograde and retrograde satellite orbits. In all MEGNO maps, we chose to colour code initial conditions resulting in quasi-periodic motion by blue (see the electronic version of this work). In the quasi-periodic case, our numerical experiments typically show  $|\langle Y \rangle - 2.0| < 0.01$  at the end of the numerical integration. In addition, we also provide maps showing the maximum semimajor axis (MS) and maximum eccentricity (ME) of an orbit at a given initial grid point. MS and ME maps were constructed in parallel with the MEGNO calculations (Goździewski 2002). The osculating elements of the satellite were measured at each completed Jovian period (equivalent to the renormalization time) and the maximum value is determined by comparing with a previous measurement.

#### 5 SMOOTHING ORBITAL ELEMENTS

To study the secular evolution of irregular satellites numerically, we have to filter out the fast frequencies. Saha & Tremaine (1993) already pointed out that the unfiltered variations in the action elements (semimajor axis, eccentricity and inclination) are larger than the filtered time series of a given element. This means that the fast variations (high-frequency terms) are much larger in amplitude than the slow variations (long-period terms). Hence, the secular evolution is masked by the high frequencies. In this work, an initial preliminary study of several test orbits confirmed this dynamical behaviour, and we find that the most interesting dynamical features are to be found in the secular evolution. To obtain the secular evolution, one can either average out the fast frequencies by applying a digital filter in either the time or frequency domain (Carpino, Milani & Nobili 1987; Quinn, Tremaine & Duncan 1991; Saha & Tremaine 1993; Michtchenko & Ferraz-Mello 1995; Nesvorný & Ferraz-Mello 1997) or by averaging out all quasi-periodic oscillations with a running window average (Morbidelli 1997; Morbidelli & Nesvorný 1999; Tsiganis, Varvoglis & Hadjidemetriou 2002). We chose the latter method as it is more straightforward to implement.

In order to study the satellites secular evolution, we smooth the orbital elements of a given time sequence  $A_i$  using the `smooth` function as implemented in Interactive Data Language (IDL).<sup>5</sup> The smoothing procedure is a running window average applied on the full data set as obtained from a numerical integration. The output of a given numerical integration is given as a time sequence of orbital elements sampled at regular intervals of length  $\Delta T$ . For a given sequence of an orbital element,

$A_i = A(t_i)$  with  $t_i = t_0 + i \Delta T$  (for  $i = 0, 1, \dots, N$ ) the smoothed (secular) sequence  $R_i$  is given by

$$R_i = \begin{cases} \frac{1}{w} \sum_{j=0}^{w-1} A_{i+j-(\frac{w-1}{2})}; & i = \frac{w-1}{2}, \dots, N - \frac{w+1}{2} \\ A_i & \text{otherwise.} \end{cases}$$

Here,  $N$  is the number of data points from the numerical integration, and  $w$  is the (running) window width over which the original data set is averaged. In units of time, the window width is  $w \Delta T$ . The window width represents a free parameter and basically controls the suppression of dynamical features seen in the data set. Too short a window will have little smoothing effect and thus the fast

<sup>5</sup> For more information <http://www.itavis.com/ProductServices/IDL.aspx>.

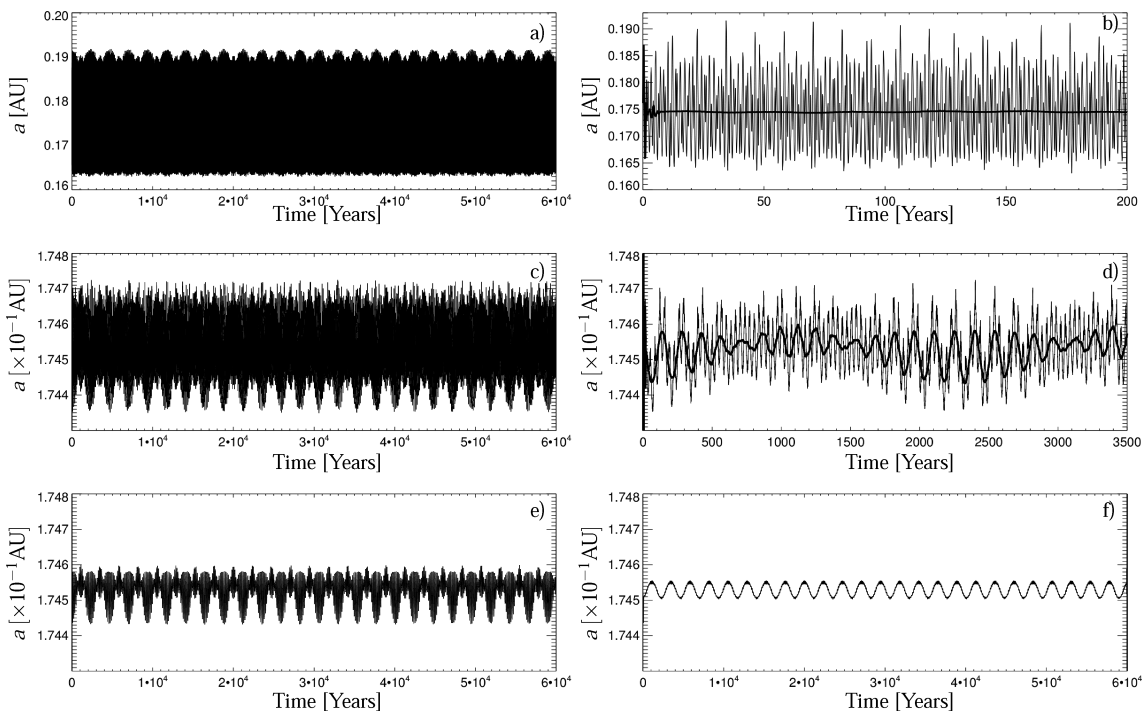


**Figure 7.** Demonstrating the process of successive smoothing using a running window time average applied on the semimajor axis. See text for details.

frequencies are retained. Too large a window width will suppress long-period features that appear on secular time-scales. In practice, some non-quantitative empirical experimentation is needed in order to determine a satisfying window width. In this study, we have performed an extensive survey of various window widths. In each plot showing smoothed orbital elements, we have chosen the most appropriate window width in order to highlight the secular changes of a particular orbit.

Some care has to be taken when smoothing angular variables. As already mentioned by Saha & Tremaine (1993) filtering (or smoothing), an angular variable is problematic as angles may change discontinuously over the time sequence (i.e. from  $-\pi$  to  $\pi$ ). Applying a running window smoothing procedure directly to an angular variable introduces spurious results around discontinuities. To circumvent this problem, we transform a given angular variable to a continuous signal. Let  $\theta$  be an angular variable changing discontinuously at times during the numerical integration. Then we transform to the following continuous variables,

$$p = A \cos(\theta), \quad (18)$$

$$q = -A \sin(\theta), \quad (19)$$

where  $A$  is some suitable constant. Here, we chose  $A = 1$ . The IDL SMOOTH smoothing procedure is then applied to each of the quantities  $p$ ,  $q$  and we obtain  $\bar{p}$ ,  $\bar{q}$  after which we obtain the smoothed angle  $\bar{\theta}$  from  $\bar{\theta} = \arctan(\bar{q}/\bar{p})$ .

An important note about the SMOOTH routine is the following. The averaging behaviour at the beginning and end of the original time sequence depends on the optional EDGE\_TRUNCATE keyword passed to the SMOOTH function. If this keyword is enabled, the smoothing procedure might introduce false/misleading averages at the beginning and end of the smoothed signal. Details can be found in the IDL documentation. In addition, if this keyword is disabled then it is important to note that  $R_i = A_i$  for the first data points up to (but not

including)  $(w - 1)/2$  and  $R_i = A_i$  from  $N - (w + 1)/2$  (but not including) to  $N$ .

We demonstrate the effect of successively applying time-averaging smoothing windows to the time evolution of the semimajor axis in Fig. 7. Fig. 7(a) shows the whole signal over 60 000 yr with a sampling frequency of 40 d. At this stage, a secular period of about 2400 yr is clearly present in the frequency spectrum of the signal. Fig. 7(b) shows the first 200 yr of the full data set (thin line) which is dominated by the orbital frequency of the satellite and an approximately 12-yr period (Jupiter's orbital period). When applying two successive smoothing windows to the raw data with window width 3 and 12 yr, we obtain the average signal overplotted as a thick line in Fig. 7(b). Fig. 7(c) zooms in on the smoothed signal over the whole integration time (note the difference in range of the semimajor axis). Fig. 7(d) (thin line) shows the first 3500 yr of the previous signal. This time we detect a 34-yr periodicity in the semimajor axis. Applying a smoothing window removes the 34-yr period [thick line in Fig. 7(d)] and the smoothed signal over the 60 000 yr is shown in Fig. 7(e). Furthermore, a 140-yr period signal is present in the semimajor axis as shown in Fig. 7. Applying a fourth smoothing window to the original raw signal now also removes this period and we end up with the secular signal (2400-yr period) shown in Fig. 7(f). All periods have been determined by visual inspection from the graph by dividing the total time-span in a given graph with the number of periods readily countable in the signal. At this stage, we are not interested in a detailed frequency analysis; our main concern is to isolate the secular system.

In Fig. 8, we show examples of the effect of the smoothing procedure when applied to the numerical solution of two different initial conditions located close to each other in  $(a, I)$  space. In both panels, we show the semimajor axis, eccentricity, inclination and the angle  $\varpi - \varpi_\odot$  for each initial condition. The left-hand (right) panel is the result of integrating initial condition IC-I (IC-II) as indicated in Fig. 9. Each orbit was integrated for 60 000 yr, the integration length of each grid point in the MEGNO maps. The black bars

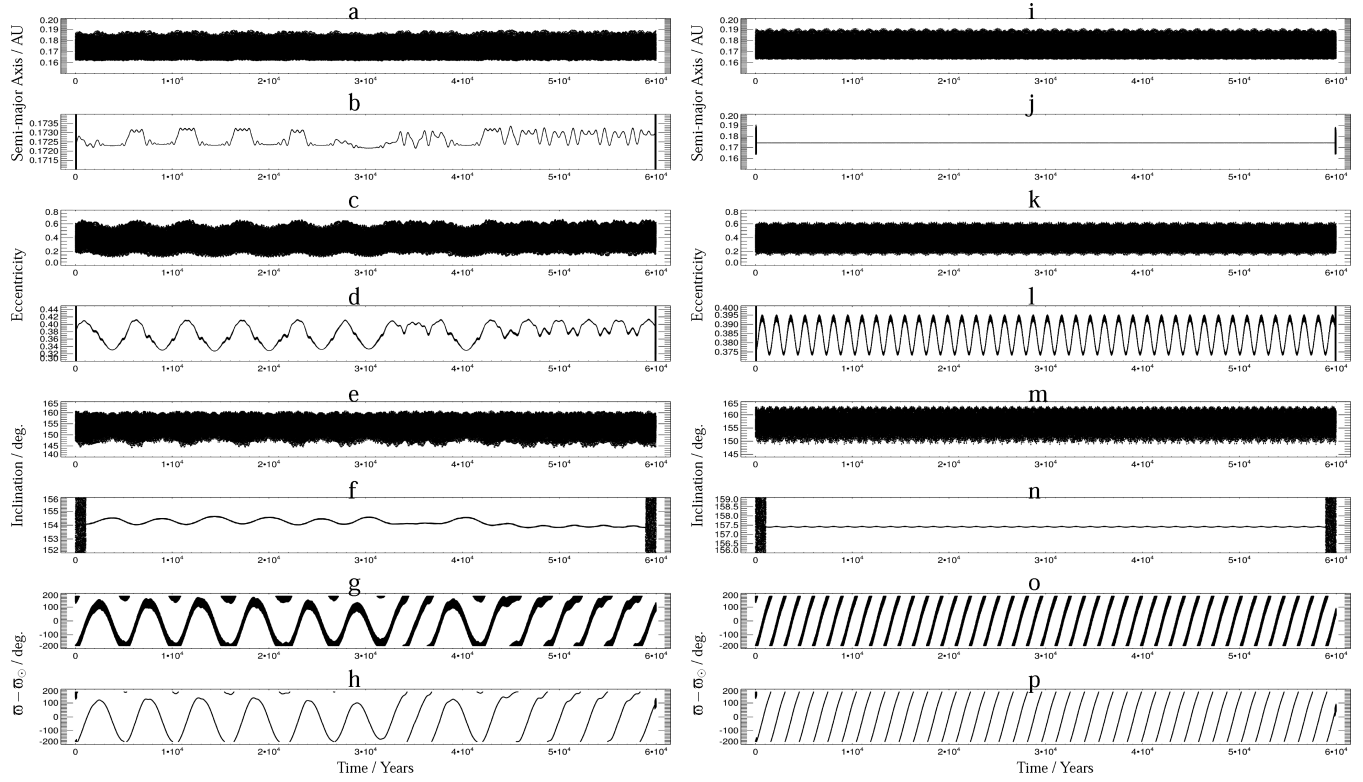


**Figure 8.** Time evolution of orbital elements for initial condition IC-I (left-hand panel, chaotic) and initial condition IC-II (right-hand panel, quasi-periodic). The full data set (panel a, c, e and g) and corresponding smoothed data set (panel b, d, f and h) are shown in each panel. From top to bottom panel: semimajor axis (a+b). Eccentricity (c+d). Inclination (e+f) and the angle  $\varpi - \varpi_{\odot}$  (g+h). The smoothing window applied to the data set in both panels are identical. Only the initial conditions have changed. Half of the window widths for a given element can be seen as a black bar at the beginning and end of the integration time. Each initial condition has been integrated for 60 000 yr corresponding to the integration length in the MEGNO maps. The window widths are  $w/2 \times \Delta T = 2500/2 \times 40$  d = 137 yr for panels b, d, h and  $w/2 \times \Delta T = 20000/2 \times \Delta T = 1095$  yr for panel f. Note that  $\varpi_{\odot} = \varpi_J - 180^\circ$ .

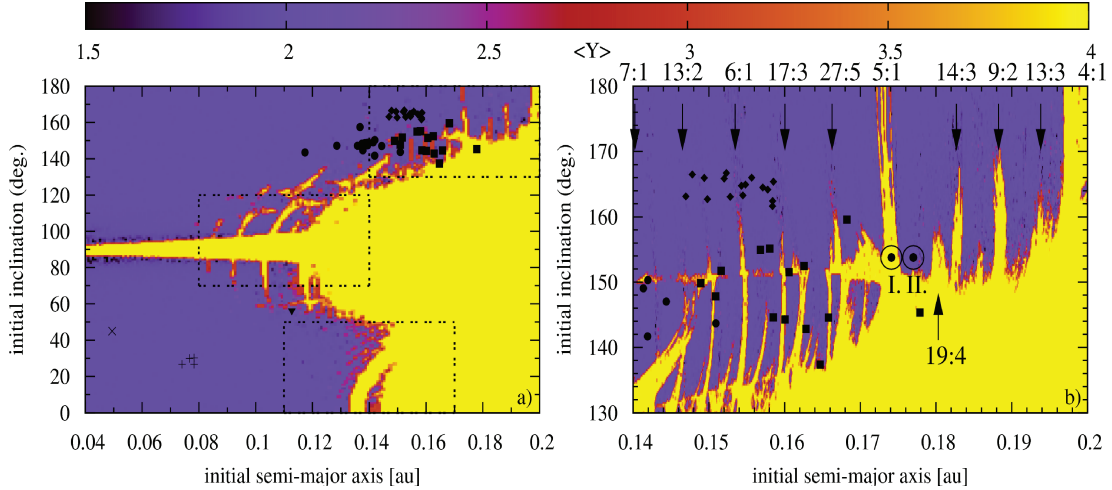


**Figure 9.** MEGNO maps in (a, I) space of test satellites with  $e_0 = 0.20$ ,  $\omega_0 = 0^\circ$ ,  $\Omega_0 = 0^\circ$ ,  $M_0 = 90^\circ$ . The MEGNO indicator  $\langle Y \rangle$  is colour coded on a linear scale from 1.5 to 4 with  $\langle Y \rangle = 2$  indicating quasi-periodicity and  $\langle Y \rangle = 4$  denoting chaotic initial conditions. See the electronic version for colours. In both panels, the symbols denote locations of irregular satellites. Themisto is at 0.05 au ( $0.14 R_H$ ,  $105 R_{Jup}$ ) and indicated by a  $\times$  symbol). Himalia family = + symbols and Carpo = (black  $\blacktriangledown$  symbol) at 0.112 au ( $0.32 R_H$ ,  $235 R_{Jup}$ ). We plot family members for which  $|e(t) - 0.20| < 0.05$ . Ananke (black  $\bullet$  symbols), Carme (black  $\blacklozenge$  symbols) and Pasiphae family (black  $\blacksquare$  symbols). Left-hand panel (a): three regions showing interesting dynamical features are shown by rectangles. Right-hand panel (b): high resolution zoom of the upper right region shown in panel (a). Arrows indicate the locations of retrograde MMR. Nominal locations are given in Table 2. Also shown are the locations (IC-I and IC-II) of two test orbits. As already detected by Yokoyama et al. (2003) note the small stable region at  $(a_0, I_0) = (0.142$  au,  $10^\circ$ ).

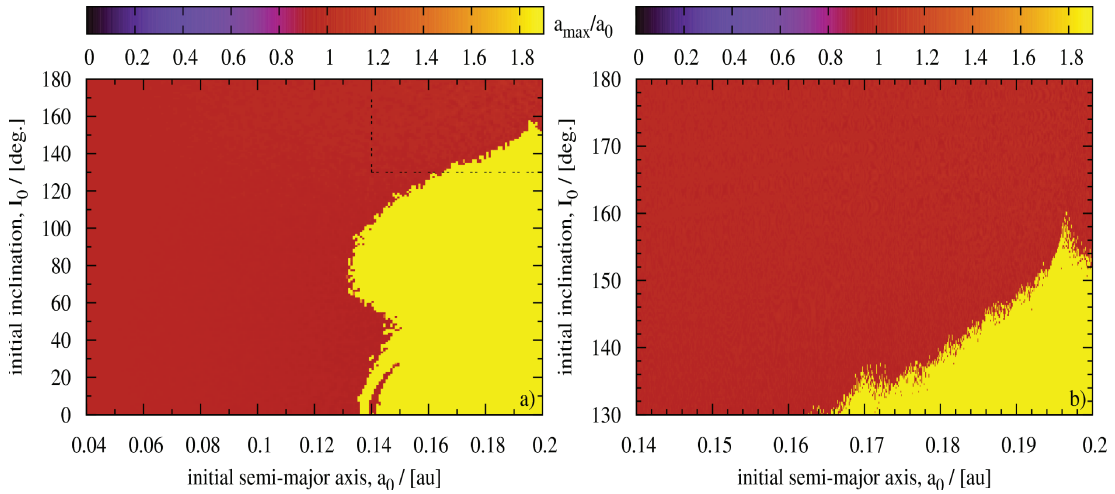


**Figure 10.** Maps plotting the ratio  $a_{\max}/a_0$  of a given initial condition in  $(a_0, I_0)$  space for an irregular test satellite. Left-hand panel (a): same range in semimajor axis and inclination as for the MEGNO map. A ratio of  $a_{\max}/a_0 \sim 1.9$  indicates orbits close to the Jovian Hill radius (0.355 au) corresponding to escape orbits. Right-hand panel (b): high-resolution zoom of the rectangular area as indicated in the left-hand panel (a). In both panels, the initial semimajor axis does not change significantly (i.e.  $a_{\max}/a_0 \sim 1.0$ ).

(or sometimes scattered data points) show half the window width (see figure caption for more details) and has been empirically determined based on qualitative judgment with the goal to enhance the underlying dynamical changes in a given osculating element. As already pointed out in Saha & Tremaine (1993), we again observe that most of the variation in the orbital elements are found in the fast frequencies. A visual inspection of the time evolution of initial condition IC-I confirms its chaotic nature as correctly identified by MEGNO. For comparison, a time-running window with identical window width has been applied to initial condition IC-II. Its quasi-periodic nature is clearly visible over the considered time-span. From experimentation with the window width, we observed that increasing the width averages out more and more quasi-periodic oscillations. No chaotic behaviour has been observed when increasing the window width. Following Morbidelli & Nesvorný (1999, p.301) and Tsiganis et al. (2002), by applying a time-running window smoothing procedure to a given osculating element, we obtain an approximation of the corresponding *proper element*. If the orbit evolves quasi-periodically (regular motion with a limited number of frequencies) in time then the corresponding proper element is a constant of motion. On the other hand, if the corresponding proper element is chaotic then it exhibits a random walk in time. The chaotic nature of integrating initial condition IC-I particularly manifests itself in the time evolution of  $\varpi - \varpi_\odot$  as shown in Fig. 8(h) (left-hand panel). This angle repeatedly changes from libration to circulation; this is characteristic of chaotic behaviour (as in the perturbed pendulum model). For comparison, this angle circulates for initial condition IC-II (quasi-periodic) over the entire integration time-span without any change in oscillation mode.

## 6 RESULTS AND DISCUSSION

### 6.1 MEGNO, $a_{\max}$ and $e_{\max}$ maps

Our results on computing the MEGNO indicator over a large grid in  $(a_0, I_0)$  space are shown in Fig. 9. This figure shows the grid  $(a_0, I_0) \in ([0.04, 0.20] \text{ au}, [0^\circ, 180^\circ])$ . The observed population of prograde and retrograde satellites are shown by various symbols (see figure caption for details). We obtained the osculating elements of

the irregular satellites from the JPL Horizon Ephemeris system (see earlier section on initial conditions). We chose to consider this part of phase space in order to compare with previous results as published by Carruba et al. (2002)<sup>6</sup> and Yokoyama et al. (2003). These authors explore similar phase-space regions although they consider a much coarser grid of initial conditions. Reproducing previously published results motivated us to apply and compute the MEGNO indicator over a much larger region occupied by the outer irregular Jovian satellites. In our work, at initial time the eccentricity was set to  $e_0 = 0.20$  and the remaining Kepler elements ( $\omega_0, \Omega_0$ ) were set to zero with  $M_0 = 90^\circ$ . We calculated the MEGNO indicator for 35100 initial conditions  $(N_x, N_y) = (195, 180)$ . The orbit corresponding to each initial condition was integrated for  $5 \times 10^3 P_J \text{ yr}$  ( $P_J$  is the orbital period of Jupiter).

To save computing time, we stopped a given integration as soon as  $\langle Y \rangle \geq 10.0$ . The MEGNO indicator is then colour coded with  $\langle Y \rangle = 2.0$  indicating quasi-periodic motion and we only plot  $\langle Y \rangle \leq 4$  to enhance the contrast of dynamical features in the transition region where the dynamics change from quasi-periodic to chaotic. Fig. 9(a) shows several interesting regions of chaotic and quasi-periodic nature with unprecedented detail. We decided to compute high-resolution maps to study this interesting region. A zoom plot is shown in Fig. 9(b) and corresponds to the area within the box in the upper right corner of Fig. 9(a). The labels IC-I and IC-II correspond to initial conditions for two hypothetical (retrograde) irregular satellites.

In parallel with computing  $\langle Y \rangle$  to detect chaos, we also recorded the maximum values of the test satellites' semimajor axis and eccentricity every orbital period of the Sun. Figs 10 and 11 show the corresponding maps. It is now apparent that the global chaotic region results in either escape or collisions after only  $5 \times 10^3 P_J \text{ yr}$ . From this result, we can conclude that the large chaotic region detected in the MEGNO map is strongly correlated with either escape from the Jovian Hill sphere or collisions with Jupiter itself. It is also interesting to note that over a large range the orbit size (semimajor

<sup>6</sup> The authors use different units for the semimajor axis. Carruba et al. (2002) measure distance in units of Jupiter's Hill radius  $R_H$ , and Yokoyama et al. (2003) measure distance in units of Jupiter's radii  $R_{Jup}$ .

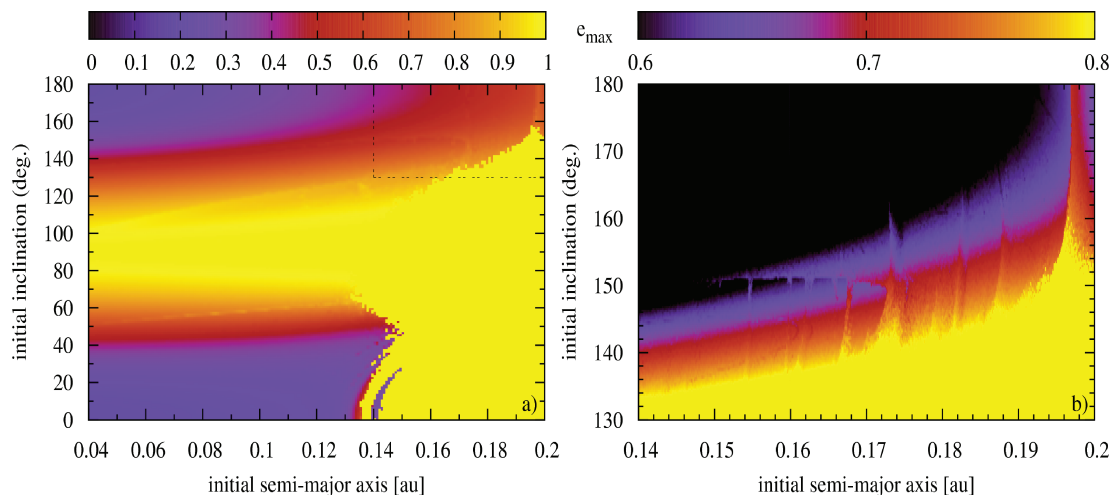


**Figure 11.** Same as Fig. 10 but using  $e_{\max}$  for the colour coding. Note the horizontal feature of enhanced eccentricity for both pro- and retrograde satellites. This feature was also reported to exists from a 1 Myr integration (fig. 6 Yokoyama et al. 2003). In panel (b), the dark (black) region indicates  $e_{\max} \leq 0.6$ .

axis) remains close to its initial value. Furthermore, we also note that the locations of mean motion resonances are not visible in the zoom plot [Fig. 10(b)] as otherwise indicated by MEGNO. This indicates that the semimajor axis is unaffected by the presence of mean motion resonances and MEGNO is efficient in detecting mean motion resonances. A different picture is obtained when studying the ME attained during a numerical integration of a test satellite. Fig. 11 shows a clear dependence of  $e_{\max}$  with inclination. In a later section, we will study and discuss the time evolution of these initial conditions to unravel their chaotic and quasi-periodic nature in detail presenting a proof of concept of detecting chaotic initial conditions. In this work, we will discuss the location of mean motion resonances and postpone the study and discussion of other features (boxes located at polar and prograde orbits) in a future work.

### 6.1.1 Choice of integration time

Up to now, we have left unanswered the question regarding the choice of minimum motion time to integrate the dynamical system. For how long has a given orbit to be integrated in order to reveal chaotic regions as ‘saturated’ in a MEGNO map? As mentioned earlier in the  $N$ -body problem initial condition initially in quasi-periodic phase space regions can only be proven to be regular up to the maximum integration time for which  $\|\langle Y \rangle - 2\| \sim 0$ , while other initial conditions render the orbit to be unequivocally chaotic after some time for which  $\langle Y \rangle \gg 2.0$ . By saturation, we mean a maximum time after which  $\langle Y \rangle(t)$  no longer changes [e.g. the 17:3 MMR in Figs 12(A)–(C)]. What is the minimum integration time? We have tried to answer this question by generating different one-dimensional (possibly high resolution) MEGNO maps for increasing integration length or motion times of the system. A more detailed inspection of Fig. 9 suggests that the chosen integration time (60 000 yr) is too short to saturate  $\langle Y \rangle$  in the MEGNO map to reveal the presence of high-order MMRs (e.g. 6:1, 17:3, 27:5) for low retrograde inclinations ( $I > 160^\circ$ ). Since computing high-resolution MEGNO maps is computationally time intensive when increasing the integration time we have computed three one-dimensional slices at constant retrograde inclination ( $I = 160^\circ, 165^\circ, 170^\circ$ ) while scanning through the semimajor axis ( $a \in [0.14, 0.20]$  au). Orbits in each slice were computed considering three dif-

ferent motion times ( $T_{\max} = 60\,000, 120\,000$  and  $300\,000$  yr). We show our results in Figs 12 and 13.

Considering the case with  $I = 160^\circ$ , it is evident that  $\langle Y \rangle$  continues to increase for the most prominent resonances the larger the considered motion time. What consequence does this have when presenting our MEGNO maps? Considering the 6:1 MMR in Fig. 9 with  $\langle Y \rangle \sim 3.0$  at  $I \sim 160^\circ$  our result would suggest that this part of the resonance has not yet saturated after 60 000 yr, and  $\langle Y \rangle$  would increase when integrating for a longer motion time. Specifically from Fig. 12(A)–(C), increasing the motion time increases  $\langle Y \rangle$  from  $\sim 3.0$  to  $\sim 23$  for the 6:1 MMR. A similar discussion would apply to the 27:5 MMR. However, it is important to note that the 7:1, 13:2, 17:3 and 19:4 MMR reveal no significant changes in  $\langle Y \rangle$  when studying progressively longer motion times. We can conclude that using a motion time of 60 000 yr these resonances appear as saturated in our MEGNO map and will have little dynamical influence on the dynamics of satellites with low-inclination retrograde orbits ( $I > 160^\circ$ ).

Since the Ananke family is clustered between  $I = 160^\circ$  and  $170^\circ$ , we ask the question what is the minimum retrograde orbital inclination at which the 6:1 MMR reveals its chaotic character? Studying the case  $I_0 = 165^\circ$ , we show our results in Figs 12(D)–(F) for increasing integration times. Since the 6:1 MMR is no longer present at  $a = 0.155$  au. This suggests that irregular satellite members of the Ananke family are dynamically unaffected by this resonance. Furthermore, the width of a given MMR indicates its saturation. To illustrate, this we refer the reader to the 27:5 and 14:3 MMR in Figs 12(D)–(F). Finally, we observe that only the 5:1 and 9:2 MMRs exist when increasing the retrograde orbital inclination to  $I_0 = 170^\circ$ . We conclude this section by noting that the maximum integration time is a trade-off between resolution of the MEGNO map and computing time. Our choice of the maximum integration time of 60 000 yr is sufficient to reveal and detect the location of prominent MMRs while pointing out that some one-dimensional (possibly high-resolution) test maps might be necessary to be computed considering prolonged integration times of the system.

### 6.2 Fine structure: mean-motion resonances

Fig. 9(b) shows details of the retrograde region with  $a \in [0.14; 0.20]$  au ( $[0.39, 0.56] R_H, [293, 419] R_{Jup}$ ) and  $I \in [130^\circ; 180^\circ]$ . Several

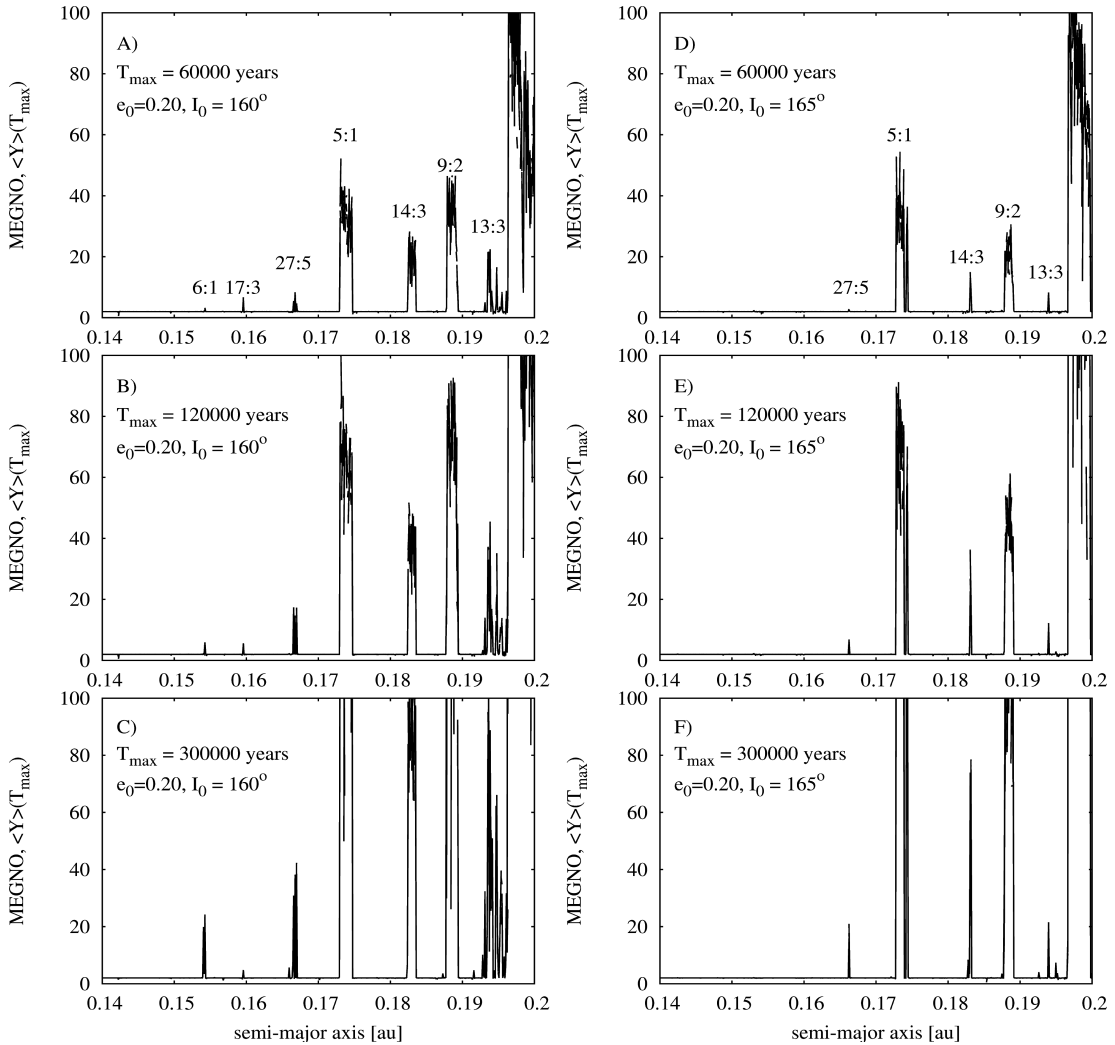


**Figure 12.** One-dimensional MEGNO maps showing the dependence of  $\langle Y \rangle$  on the maximum integration time ( $T_{\max}$ ) for two different retrograde orbital inclinations. Left-hand panels (A–C):  $I_0 = 160^\circ$ . Right-hand panel (D–F):  $I_0 = 165^\circ$ . Both panels should be compared with Fig. 9. Identical initial conditions were used. Integration time increases from top to bottom. The top panels indicate the location of most dominant MMR. The semimajor axis has the same resolution as the two-dimensional MEGNO map as shown in Fig. 9.

vertical structures are observed corresponding to the location of MMR. If  $n$  and  $n_J$  denotes the mean-motion of the satellite and Jupiter, respectively, then the semimajor axis of a satellite in a  $n : n_J$  MMR with Jupiter is given by

$$a_s = a_J \left( \frac{n}{n_J} \right)^{-2/3} \left( \frac{m_J + M_\odot}{m_J} \right)^{-1/3}, \quad (20)$$

where  $a_J, m_J$  denote Jupiter's semimajor axis and mass, respectively.  $M_\odot$  is the mass of the Sun. In the above expression, the subscripts  $J$  and  $\odot$  are interchangeable. In Fig. 9(b), we show the location of several of these resonances with arrows and list their locations in Table 2. Several high-order MMRs are detected close to observed clusters of irregular satellite families.

When compared to the current population of observed irregular satellites, it is interesting to note the large scatter in  $(a, I)$  elements of the Pasiphae group. Fig. 9(b) strongly implies that several members of this group are strongly affected by the dynamics within high-order MMRs. The dynamical consequences of MMRs on the orbits of irregular satellites were already reported by Saha & Tremaine

(1993) discussing the  $n - 6n_J \sim 0$  resonance of Sinope and possibly Aitne (previously labelled S/2001 J11) (Nesvorný et al. 2003). Showing a more compact distribution of the osculating elements, members of the Carme family are on less inclined orbits  $I \sim 165^\circ$ . It appears that the dynamical effects of the MMRs occur at a smaller magnitude for this group possibly resulting in a smaller dispersion in orbital elements. In addition, the Ananke group shows also a small scatter in their orbital elements possibly due to the close proximity of the 7:1 MMR. The coincidence between the scatter of orbital elements of retrograde satellites and the presence of MMRs is probably not by chance. We stress that this work does not address the dynamical significance and effects of MMRs, but raises the question of the dynamical effects of these MMRs on the orbital elements of a compact group of satellites. Therefore, we hypothesize the possibility of orbital scattering by MMRs for retrograde Jovian irregular satellite families. We will address this question in a future work by studying the time evolution of orbital elements of an initial compact group of satellites by gravitational scattering in high-order MMRs.

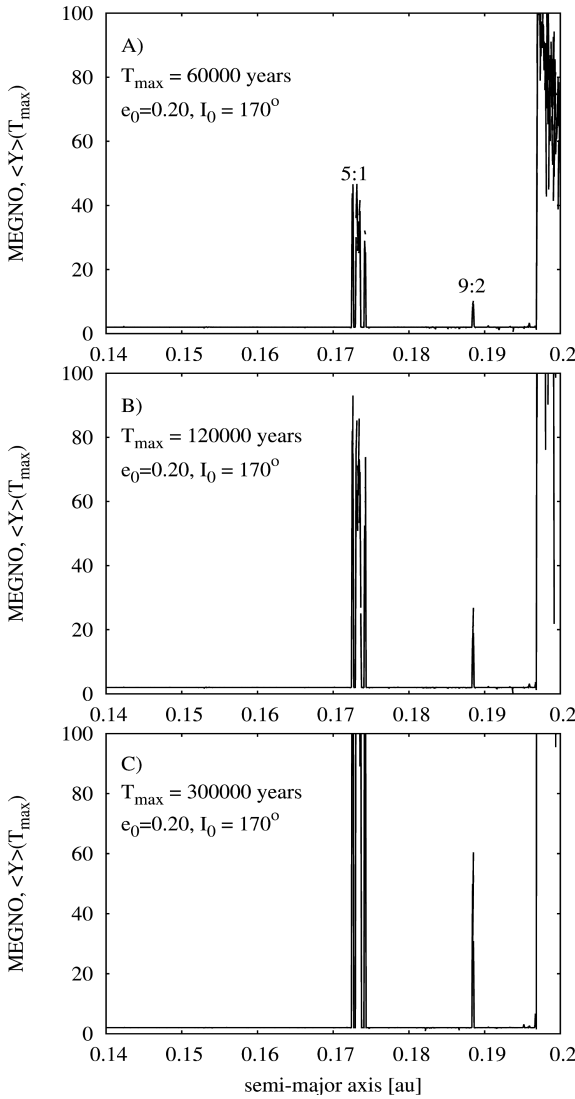


Figure 13. Same as Fig. 12 with  $I_0 = 170^\circ$ .

### 6.3 Chaotic regions and Kozai mechanism

From the MEGNO map [Fig. 9(a)], we observe a clear distinction between quasi-periodic and chaotic phase-space regions. The global chaotic region for prograde satellites starts at  $a = 0.14$  au ( $0.39R_H$ ,  $293R_{Jup}$ ) and outwards. Stable quasi-periodic orbits for the retrograde satellites are found for orbits with semimajor axis up to  $0.195$  au ( $0.55R_H$ ,  $409R_{Jup}$ ). It is interesting to note that the chaotic phase space of prograde satellites is larger when compared to the retrograde satellites. This asymmetry in  $(a, I)$  space was already discussed by Nesvorný et al. (2003) pointing out the difference between prograde and retrograde stability limits. At larger semimajor axis, the retrograde satellites are on dynamically more stable orbits when compared to the prograde irregular satellites. In this work, the calculated MEGNO map confirms this stability asymmetry which is mainly explained by the existence of the ejection resonance for prograde satellites (Nesvorný et al. 2003; Yokoyama et al. 2008, and references therein). In geometrical terms, this resonance locks the satellites apocentre towards the direction of the Sun and maintains this alignment for a period of time. In this orbital configuration solar perturbations accumulate and the satellite eventually escapes from Jupiter when  $\varpi - \lambda_\odot \sim 0$ . An interesting feature shown in the

map is the chaotic horizontal ‘cone’ for polar orbits at around  $I \sim 90^\circ$  extending from  $a = 0.04$  au ( $0.11R_H$ ,  $84R_{Jup}$ ) to  $a = 0.12$  au ( $0.34R_H$ ,  $251R_{Jup}$ ). This region was already studied intensively by Carruba et al. (2002) and Nesvorný et al. (2003) showing that test satellites with inclinations in the range  $70^\circ < I < 110^\circ$  have orbits with survival times less than  $10^7$  yr. Analytical perturbation theory (Carruba et al. 2002) showed that the accumulation of secular solar perturbations is the driving force causing the excitation of orbit eccentricity to large values. This mechanism is known as the Kozai resonance. Depending on the initial value of  $\varpi$  circular orbits can reach high eccentricities and collisions with the inner regular satellites (or with Jupiter itself) are expected to occur. Thus, the Kozai resonance provides an efficient dynamical mechanism to remove an initial population of near-polar irregular satellites. When studying Fig. 11, we note that the Kozai regime is well identified with large eccentricities attained in the range  $40^\circ < I < 140^\circ$ . However, it needs to be mentioned that the eccentricity excitations might strongly depend on the initial  $\varpi$  (Carruba et al. 2002).

### 6.4 Chaoticity versus quasi-periodicity

Previously, we have reported on the presence of chaotic dynamics as detected from calculating  $Y$ ,  $\langle Y \rangle$  on a grid of initial conditions in  $(a, I)$  space. In the following, we will study in detail two initial conditions that were detected to be either quasi-periodic or chaotic. Fig. 9 marks the two initial conditions by dots (surrounded by circles) with IC-I and IC-II. Both initial conditions have the same orbit inclinations but different semimajor axes. We refer to Table 1 for the numerical values of our initial conditions. We have then numerically integrated both orbits using the RADAU integrator (as implemented in the MERCURY package) with initial step size of 0.01 d and tolerance parameter of  $10^{-13}$ . This approach provides an independent check on chaotic/quasi-periodic orbits as computed from MEGNO. Calculations were done in double precision. Initial conditions for the Sun were obtained from the JPL Horizon ephemeris system (Giorgini et al. 1996). We sampled osculating elements every 40 d. To maintain consistency with the MEGNO calculations using the GBS algorithm, we integrated the orbits over 60 000 yr ( $5 \times 10^3 P_J$ ). For both orbits, the maximum relative energy error at the end of integration was smaller than  $10^{-13}$ .

#### 6.4.1 Chaotic case: IC-I

As suggested from MEGNO initial condition IC-I exhibits chaotic behaviour. We present the results of our single orbit calculation in Figs 14 and 15. We have obtained those figures by successively applying the running window time average smoothing technique as outlined previously. In addition to the orbital elements  $(a, e, I)$ , we also plot the time variation of  $\varpi - \varpi_\odot$  along with four critical angles  $\phi_1, \phi_2, \phi_3, \phi_4$  (see details in the figure caption). In the bottom panel of Fig. 14, we also show the time evolution of  $Y, 2(Y)$

**Table 1.** Initial conditions for the two test satellites IC-I and IC-II in and close to the 5:1 MMR as shown in Fig. 9. The remaining Kepler elements were set to  $\omega_0 = 0^\circ$ ,  $\Omega_0 = 0^\circ$  and  $M_0 = 90^\circ$ . CH and QP denote initial conditions in the chaotic region and quasi-periodic region, respectively.

Initial conditions	$a_0$ (au)	$e_0$	$I_0$ ( $^\circ$ )	Region
IC-I	0.173915	0.20	153.968	CH
IC-II	0.176179	0.20	153.968	QP

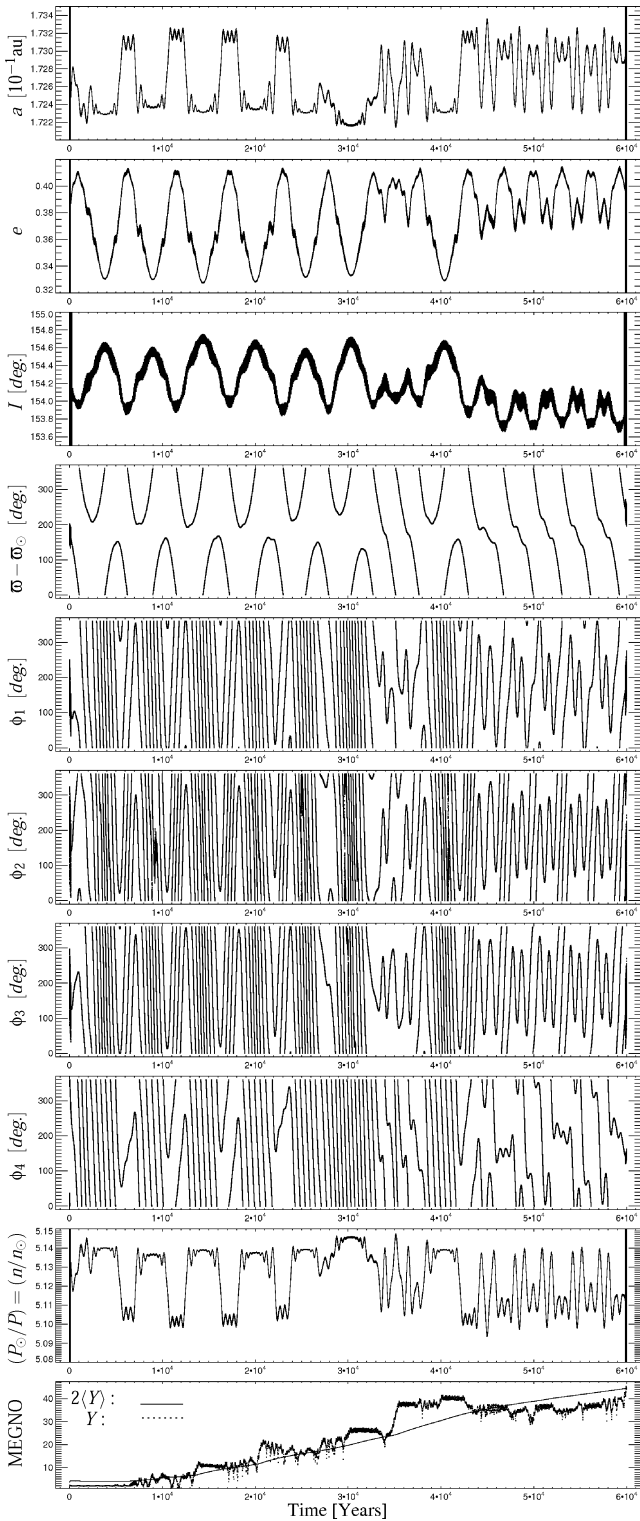


**Figure 14.** Secular time evolution of osculating elements from integrating IC-I. Elements  $a$ ,  $e$  were smoothed using a window width of  $w \times \Delta T = 2500 \times 40$  d = 274 yr. For the inclination  $I$ , we used  $w = 5000$ . The black vertical bars show half of the window width. The elements  $\varpi$ ,  $\lambda$  denote the (retrograde) longitude of pericentre and mean longitude of the satellite, respectively.  $P$  measures the orbital period of the satellite and  $P_\odot$  is the orbital period of the Sun in the Jovicentric system.  $n$  measures the corresponding mean motion. Note the linear trend of  $2\langle Y \rangle$  as predicted by the theory.  $\phi_1 = 5\lambda_\odot - \lambda - 4\varpi_\odot$ .  $\phi_2 = 5\lambda_\odot - \lambda - 2\varpi_\odot - 2\varpi$ .  $\phi_3 = 5\lambda_\odot - \lambda - \varpi_\odot - \varpi - 2\Omega_\odot$ .  $\phi_4 = 5\lambda_\odot - \lambda + 2\varpi - 6\Omega_\odot$ .

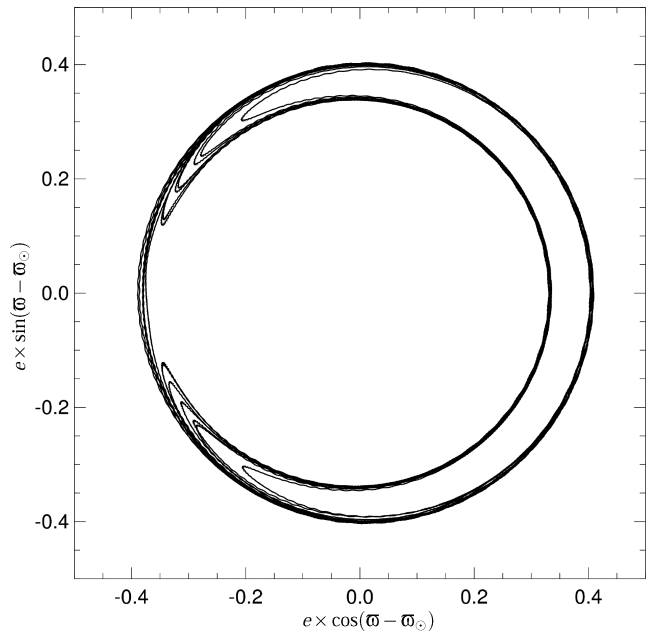


**Figure 15.** Polar representation of the temporary circulation and librations of  $\varpi - \varpi_\odot$  about  $0^\circ$  ( $\varpi - \varpi_J = 180^\circ$ ) in the 5:1 MMR of IC-I. The outer radius corresponds to  $e \sim 0.33$  and the inner radius corresponds to  $e \sim 0.41$ . The alternation between libration and circulation is a clear sign of chaotic dynamics.

as a function of time as obtained from a GBS integration (using same computer architecture as the single-orbit RADAU integration). This time we chose to plot  $2\langle Y \rangle$  to demonstrate that this quantity increases at the same rate as  $Y$  although the variation is smoother (after the onset of chaos) due to averaging. Quantitatively at time 60 000 yr, the quantity  $2\langle Y \rangle \sim 40$  and the divergence of  $\langle Y \rangle$  from 2.0 are evident. The presence of chaos is qualitatively best seen in the time evolution of the angle  $\varpi - \varpi_\odot$ . In Fig. 15, we give a polar representation of this angle. A similar approach was also adopted by Saha & Tremaine (1993). In the beginning, this angle librates around  $\varpi - \varpi_\odot = 0^\circ$ . After approximately 30 000 yr, this libration mode switches into circulation for a short-time period and then returns to the libration mode. At the end, the angle circulates. This qualitative change between different modes of motion is characteristic of motion near a separatrix. In the polar representation times of temporary librations are shown as ‘banana’-shape curves and circulations are indicated by full circles.

A more elongated banana corresponds to a larger libration amplitude of  $\varpi - \varpi_\odot$ . From Fig. 14, it is apparent that the libration amplitude changes with time. The initial conditions are chosen with the orbital inclination to be initially outside the Kozai resonance for which  $\omega$  of the satellite starts to librate around either  $90^\circ$  or  $270^\circ$  (Carruba et al. 2002; Nesvorný et al. 2003; Yokoyama et al. 2003). No large eccentricity variations are expected. It is important to note that the difference of the location of the libration centre found for the test satellite started at IC-I when compared to the libration behaviour of this angle for several major satellites. Saha & Tremaine (1993) and Whipple & Shelus (1993) report that for the retrograde satellites Pasiphae and Sinope the angle  $\varpi - \varpi_J$  librates about  $180^\circ$ . The difference from this work is the choice in reference system. In a heliocentric system, the angle  $\varpi - \varpi_\odot$  for IC-I would librate about  $-180^\circ$  which is consistent with the general trend as reported in Saha & Tremaine (1993).

**Table 2.** Nominal locations of retrograde MMRs as computed from equation (20). Following Murray & Dermott (2001), the satellite is in an interior MMR with the Sun given by the integer commensurability  $n/n_J = (p+q)/p$ . Here,  $p$  and  $q$  are integers, and  $q$  is the order of the resonance. The masses of Jupiter and the Sun and the semi-major axis of Jupiter are taken from Murray & Dermott (tables A.1 and A.2).

MMR ( $n : n_J$ )	Nominal location (au)	Order $q$
4:1	0.203 250	3
13:3	0.192 565	10
9:2	0.187 901	7
14:3	0.183 400	11
19:4	0.181 249	15
5:1	0.175 156	4
21:4	0.169 550	17
16:3	0.167 779	13
27:5	0.166 396	22
11:2	0.164 372	9
17:3	0.161 133	14
23:4	0.159 573	19
6:1	0.155 109	5
19:3	0.149 618	16
13:2	0.147 049	11
7:1	0.139 961	6

We have searched for important arguments in the disturbing function that are associated to the 5:1 MMR in order to contribute significantly to the amplitude. In general, the resonant angle (or critical angle) takes the form (p. 250 Murray & Dermott 2001)

$$\phi = k_1 \lambda_{\odot} + k_2 \lambda + k_3 \varpi_{\odot} + k_4 \varpi + k_5 \Omega_{\odot} + k_6 \Omega, \quad (21)$$

with  $\sum k_i = 0$  and the sum of the coefficients of the nodes,  $k_5 + k_6$  being even as is required by d'Alembert's rules. Since the amplitude in the expanded perturbing potential of the satellite is proportional to  $\propto e_{\odot}^{|k_3|} e^{|k_4|} s_{\odot}^{|k_5|} s^{|k_6|}$  [with  $s = \sin(1/2)I$ , (p. 251, 260 Murray & Dermott 2001)], low-order terms with small values of  $k_3, k_4, k_5, k_6$  are the most effective in contributing to the amplitude. This is because of  $e, e_{\odot} < 1$ . Since IC-I is near the 5:1 MMR (compare with Table 2), we have systematically explored and looked for the existence of slowly varying angles associated with the  $k_1 = 5, k_2 = 1$  MMR. Similar work is presented in (Yokoyama et al. 2003). Applying the described smoothing procedure on the resonant angle our survey verified that large ( $k_{3,4,5,6}$ ) integers are not able to produce long-period variations of the resonant angle. As a result, we have found four ( $\phi_{1,2,3,4}$ ) slowly varying resonant angles. Fig. 14 shows the result of a single-orbit integration, and we observe the following. Whenever the satellite's semimajor axis  $a$  is at maximum then  $\phi_1, \phi_2, \phi_3, \phi_4$  circulate in a prograde sense. Also whenever  $I$  is minimum (maximum) then  $e$  is maximum (minimum). Furthermore, whenever  $\phi_3$  librates around  $\pi$  then  $I$  is at a minimum and constant (at time 35 000 yr). We also observe that at the end of the time evolution of the satellite the angles  $\phi_1, \phi_2$  and  $\phi_3$  are alternating between libration around  $\pi$  and prograde circulation. At some times, we see a temporary resonance lock in  $\phi_2$  in the 5:1 MMR. It is important to note that IC-I is close to the exact 5:1 MMR. From calculating the nominal location of the 5:1 MMR (see Table 2), the exact resonance is at slightly larger semimajor axis. In exact resonance, the rate of change of the resonant angle  $\dot{\phi}$  would vanish implying that  $\phi$  is approximately constant or librating with small amplitude. This dynamical behaviour is not observed in the present work. A more detailed analysis of MMRs has yet to be undertaken aiming

to determine the libration centres for various commensurabilities of irregular satellites. Finally, we note that  $I$  and  $e$  are anticorrelated.

#### 6.4.2 Quasi-periodic case: IC-II

Turning our attention to the time evolution of the quasi-periodic orbit started at IC-II, we report on the following results. Fig. 16 shows the smoothed time evolution of the osculating elements ( $a, e, I$ ) along with  $\varpi - \varpi_{\odot}$ . In the bottom panel plot, we again plot the time evolution of  $Y, \langle Y \rangle$  over 60 000 yr. The smoothing follows the running window time average techniques as outlined previously. Contrary to the chaotic orbit the angle  $\varpi - \varpi_{\odot}$  now only circulates and the time variation of the semimajor axis, eccentricity and inclination are characterized by quasi-periodic oscillations.

Based on preceding comparative study, we conclude that MEGNO is a reliable numerical tool for detecting chaotic dynamics on short time-scales. We plan to use this tool in future work on the dynamics of irregular satellites for the major planets in the Solar system. A particular interesting subject of study would be the change of mass of Jupiter and the corresponding change in the topology structure of phase space at a given time during the growth phase of Jupiter.

#### 6.5 Comparing with previous work

In the following, we compare our MEGNO maps with numerical studies published previously in the literature. Fig. 17 shows a polar representation of Fig. 9(a) for two different values of initial eccentricities  $e_0 = 0.10$  and  $0.20$ . In Figs 17(a) and (b), the final value of  $\langle Y \rangle$  after 60 000 yr of integration time is colour coded, with yellow indicating chaotic dynamical time evolution and blue indicating quasi-periodic dynamics. The dynamical and collisional evolution of irregular satellites and their lifetimes have been studied by Carruba et al. (2002) and Nesvorný et al. (2003). We have compared Fig. 17 with the results of long-term integrations of hypothetical irregular satellites conducted by Carruba et al. (2002, figs 8 and 9). Similar studies can be found in Nesvorný et al. (2003, fig. 9). Initial conditions of test satellites studied in Carruba et al. (2002) have been superimposed by black dots in both maps following the exact array of initial conditions as presented in Carruba et al. (2002). The initial semimajor axis ranges from 0.08 to 0.20 au with spacing  $\Delta a = 0.02$  au. The initial inclination is  $35^\circ$ – $70^\circ$  for the prograde and  $110^\circ$ – $145^\circ$  for retrograde satellites with spacing  $\Delta I = 5^\circ$ . In the following discussion, it is important to stress the difference in the dynamical models used. In this work, we only consider the Sun–Jupiter test particle system without considering collisions with other bodies or ejections. Carruba et al. (2002) include the perturbative effects of the major planets and include collision and ejection criteria within Jupiter's Hill sphere. When comparing our results for prograde test satellites ( $e_0 = 0.10$ ) with (fig. 8 Carruba et al. 2002), all test particles with lifetimes less than 10 Myr ( $a_0 \geq 0.14$  au) are located in (or close to the onset of) the chaotic region shown in Fig. 17(a). Initial conditions started in the quasi-periodic region have stable orbits over 1 Gyr for low-inclination ( $I_0 \leq 50^\circ, a_0 \leq 0.12$  au) orbits to 10 Myr for high-inclination orbits ( $I_0 \geq 65^\circ, a_0 \geq 0.08$  au). It is important to note that although our MEGNO map shown in Fig. 17(a) indicates quasi-periodic dynamics for the high-inclination orbits (for  $a_0 = 0.08$ – $0.12$  au) those initial conditions are short-lived due to the presence of the Kozai cycle which opens up a route for those satellites to reach into the region of the orbits

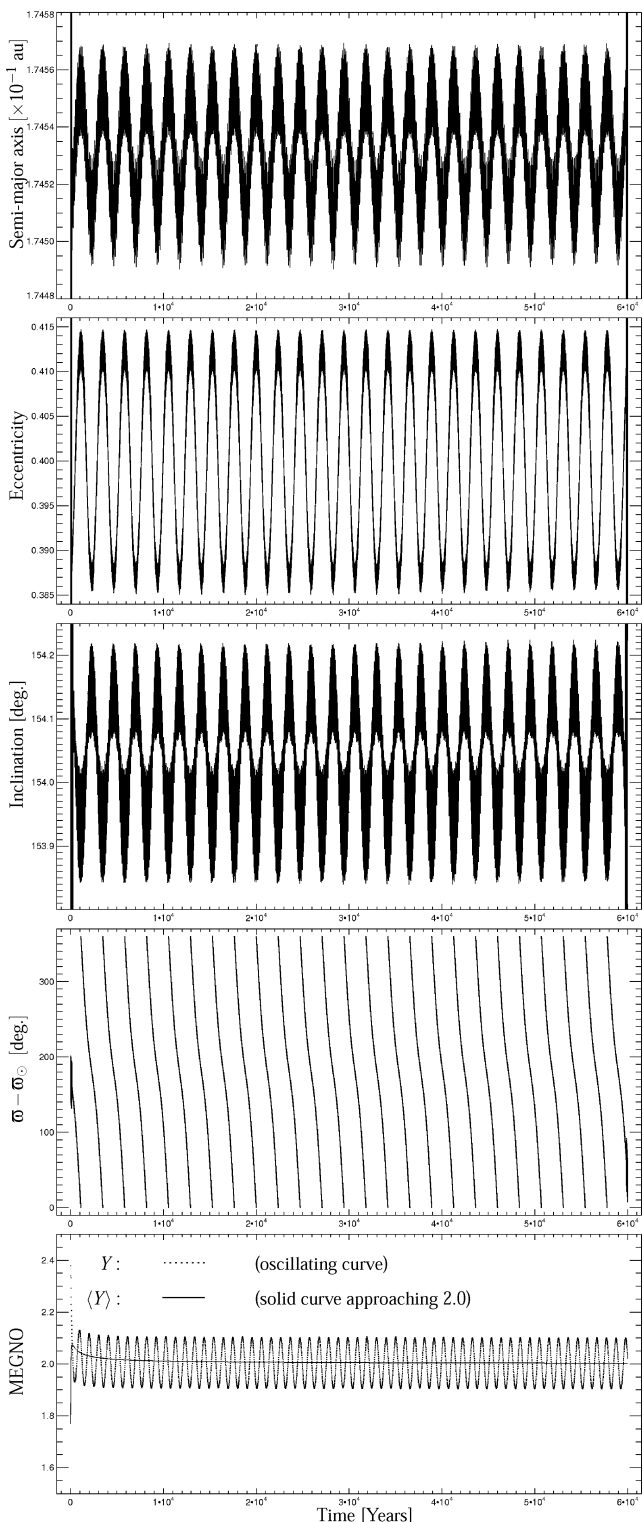


**Figure 16.** Time evolution of a test satellite with initial condition IC-II. The same window widths were used as in Fig. 14. Note the range in semimajor axis, eccentricity and inclination is smaller than in Fig. 14. This time the angle  $\varpi - \varpi_{\odot}$  is circulating as opposed to the chaotic case. For the MEGNO chaos indicator, we plot  $Y$  along with  $2\langle Y \rangle$ . From the graph, it is evident that  $\langle Y \rangle$  approaches 2.0 for the initial 60 000 yr. Specifically at the end of the integration  $\langle Y \rangle \sim 2.003$ .

of the Galilean satellites. As demonstrated by Carruba et al. (2002), such high-inclination test satellites will experience close encounters or collisions with the massive regular satellites of Jupiter. For the retrograde orbits (with  $e_0 = 0.10$ ), a comparison allows the conclusion that all test satellites started in (or close to) the chaotic region have lifetimes smaller than 1 Gyr and all test satellites with initial conditions in the quasi-periodic region have lifetimes over 1 Gyr with the exception of high-inclination orbits exhibiting Kozai cycles in their orbital eccentricities and inclinations. Similar conclusions are obtained when comparing the results shown in Fig. 17(b) ( $e_0 = 0.20$ ) with (fig. 8 Carruba et al. 2002). A final interesting point to mention is the qualitative difference in  $(a, I)$  phase-space topology of irregular satellites when varying the initial eccentricity. The prograde quasi-periodic island seen in Fig. 17(a) at  $I_0 \leq 35^\circ$  with  $a_0/R_H \times \cos(I_0) \sim 0.4$  has significantly decreased in Fig. 17(b) when  $e_0 = 0.20$ . Furthermore, the 5:1 MMR for retrograde orbits manifests itself more prominently in Fig. 17(b) when compared to Fig. 17(a). This suggests that the structure of  $(a, I)$  phase-space topology is strongly dependent on initial eccentricity.

## 7 SUMMARY, DISCUSSION AND CONCLUSIONS

In this work, we have described, illustrated and applied the MEGNO chaos indicator to the dynamics of Jovian irregular satellites. Our results are based on the numerical integration of the elliptic restricted three-body problem considering a test particle (irregular satellite) gravitationally perturbed by the Sun. No giant planet secular perturbations are present. We have deliberately considered this simplified system with the aim to isolate and identify the dynamical effects of Solar perturbations only. This approach identifies chaotic features of Jovian irregular orbits due solely to Solar tides.

The MEGNO indicator has been introduced and its various theoretical properties for regular and chaotic dynamics have been extensively illustrated by numerical examples. For a particular chaotic orbit close to the 5:1 MMR, we have computed the maximum Lyapunov characteristic number from MEGNO and compared our results with an independent standard algorithm. Based on the variational equations both numerical approaches derived the same Lyapunov time.

To support our results obtained from MEGNO, we calculated and compared the chaotic 5:1 MMR with a nearby quasi-periodic orbit. Using a different numerical integration algorithm (RADAU), we then searched for signs of chaoticity and quasi-periodicity to validate and test the results obtained from calculating MEGNO for the two initial conditions. Applying a time-running smoothing window on the osculating elements, our analysis of the single orbit computations support the results obtained from MEGNO. Initial conditions started in chaotic regions are associated to libration/circulation of resonant angles. Quasi-periodic initial conditions show circulating behaviour with no signs of alternations over the studied time interval.

Extensive numerical tests were carried out to avoid artificial numerical chaos arising from the natural time discretization of the applied numerical integration algorithms. Our tests determined an optimal choice in the absolute and relative error tolerances required in the GBS algorithm to detect real chaotic dynamics. We have calculated the MEGNO indicator for several known irregular satellites on both prograde and retrograde orbits in the framework of the elliptic restricted three-body problem. Our calculation suggests that prograde satellites are more chaotic in contrast to retrograde orbits (see Fig. 6) though the detected degree of chaoticity is very weak.

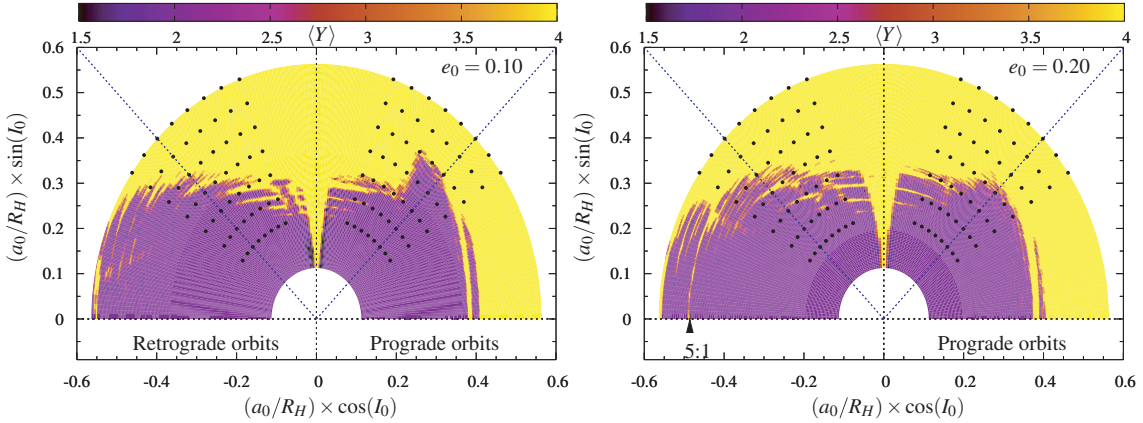


**Figure 17.** Polar representation of the  $(a, I)$  space of Jovian irregular satellites for two different initial orbit eccentricities. Left-hand panel:  $e_0 = 0.10$ ,  $\omega_0 = 0^\circ$ . Right-hand panel:  $e_0 = 0.20$ ,  $\omega_0 = 0^\circ$ . In both panels, the MEGNO indicator  $\langle Y \rangle$  is colour coded from 1.5 to 4.0 (see the electronic version for colours). The initial semimajor axis ( $a_0$ ) is given in units of Jupiter's Hill radius  $R_H$ , and  $I_0$  denotes the initial orbit inclination. The diagonal lines represent orbit inclinations at  $45^\circ$  (prograde satellites) and  $135^\circ$  (retrograde satellites). The central vertical line represents the polar orbit at  $I_0 = 90^\circ$ . For comparison, black dots indicate the more coarse initial conditions studied in Carruba et al. (2002).

It is important to note that every numerical tool capable of distinguishing between quasi-periodic and chaotic dynamics has limitations with regards to claiming quasi-periodicity considering only a limited period of time. This certainly is also the case for the MEGNO technique. In Fig. 5, we computed  $Y(t)$  and  $\langle Y \rangle(t)$  for the retrograde irregular satellite Ananke. The plot shows that after 1 Myr the orbit of Ananke exhibits a chaotic orbit with  $\langle Y \rangle(1 \text{ Myr}) \sim 4.0$ . In the 60 kyr integrations the orbit of Ananke would possibly be interpreted as quasi-periodic with  $\langle Y \rangle(t)$  deviating only slightly from 2.0. However, one-dimensional test calculations of MEGNO allowed us to conclude that several important MMRs have been saturated after considering a motion time of 60 000 yr.

Considering 35100 orbits, we calculated the MEGNO indicator on a large grid in  $(a, I)$  space known to be occupied by observed irregular satellites (Fig. 9). The resulting map revealed several interesting dynamical structures. We compared our results with previous studies addressing the question of the orbital stability of Jovian test satellites. From Fig. 17, we found good qualitative agreement between chaotic (quasi-periodic) and unstable (stable) regions as was found in previous studies (Carruba et al. 2002; Nesvorný et al. 2003). In particular, we confirm the asymmetry of the stable region when comparing prograde and retrograde satellite orbits (Nesvorný et al. 2003). Retrograde satellite orbits have access to a larger volume of phase-space characterized by orbit stability (quasi-periodicity). This result is in contrast to the prograde satellites for which chaotic orbits and their associated instability occur (for  $e_0 = 0.20$ ) at  $a \sim 0.13$  au ( $0.37 R_H$ ,  $272 R_{\text{Jup}}$ ) and onwards (cf. Fig. 9).

## 7.1 Physical results and implications from MEGNO

### 7.1.1 Prograde case

(i) From Fig. 9, no chaoticity due to high-order MMRs was detected for the prograde satellite Themisto and members of the Himalia family. This has implication that the observed velocity dispersion (Nesvorný et al. 2003) of family members has its sole origin in gravitational scattering by the largest member as hypothesized and studied by Christou (2005).

(ii) From Fig. 9, the orbit of the prograde satellite Carpo is close to the general chaotic region and close to a horizontal chaotic struc-

ture at  $I \sim 60^\circ$ . This chaotic structure coincides with a region of eccentricity excitation as shown in Fig. 11. Prolonging the integration time might enhance and reveal the true nature of this structure and is left for a future study. Since longer integration times are needed to unequivocally reveal the horizontal chaotic region, we conjecture an association of this region with a secular resonance for prograde orbits.

(iii) From Fig. 9, a quasi-periodic area at  $a \sim 0.14$  au and  $I \sim 10^\circ$  exists close to the general chaotic region. This result has been confirmed by our ME and MS maps.

(iv) The global chaotic region within Jupiter's Hill sphere is associated with either collisions with Jupiter or escape.

(v) From Fig. 9(a), we observe vertical chaotic phase-space structures associated with high-order MMRs at highly inclined orbits for semimajor axis  $a \in [0.08, 0.14]$  au. These resonances might have a dynamical significance on observed satellite orbits as they possibly reach down to the orbit of Carpo.

(vi) High-order MMRs at  $a \sim 0.14$  au and  $I \sim 30^\circ$  are observed to appear. Although no irregular satellites have been observed to exist in this region a more detailed study for longer integration times would be interesting when trying to study their effects on the orbital stability of hypothetical satellites.

### 7.1.2 Retrograde case

(i) From Fig. 9(a), we detected high-order MMRs for high polar satellite orbits with semimajor axis  $a \in [0.08, 0.12]$  au and  $I \in [90^\circ, 140^\circ]$ . The almost vertical structures seem to appear disrupted. When comparing this region with Fig. 11, we might correlate the disruption band with a region of higher eccentricities. The dynamical cause of this feature in phase space has not yet been identified.

(ii) From Fig. 9(b), we detected and identified the locations of high-order MMRs. The most prominent resonance is associated with the 5:1 commensurability. While previous studies showed that the dynamics of Sinope is characterized by the overlap of the 6:1 MMR with the secular resonance ( $\varpi - \varpi_\odot$ ) (Saha & Tremaine 1993), no irregular satellite is known to be locked into the 5:1 MMR.

(iii) Furthermore from Fig. 9, we note the coincidence of the location of high-order MMRs with the largely dispersed orbits of members of the Pasiphae family. We therefore hypothesize that

the orbital dispersion of the Pasiphae family members is a result of gravitational scattering due to MMRs. Our results support this hypothesis as the more compact Carme family is observed to be less affected by the detected resonances at lower retrograde orbital inclinations. This conjecture needs confirmation by dynamical simulations and will be tested in a separate, currently ongoing study.

(iv) From Fig. 9(b), we detect a horizontal structure at  $I \sim 150^\circ$ . This feature is also observed to be present in Fig. 11. We hypothesize that this structure is associated with a secular resonance. To reveal the more precise nature of this chaotic structure extended integration times are necessary in future studies in order to ‘saturate’ the corresponding region in  $(a, I)$  phase space as chaos possibly manifests itself on longer time-scales. A similar horizontal chaotic structure is observed at  $I \sim 60^\circ$  for prograde orbits.

Motivated by the success of applying the MEGNO technique to the dynamics of irregular satellites, we plan to conduct a large parameter survey to identify further chaotic regions within the Hill sphere of Jupiter. In addition, we plan to include giant planet perturbations and generate similar MEGNO maps of observed populations of irregular satellites in orbit around the remaining giant planets in the Solar system.

## ACKNOWLEDGMENTS

TCH acknowledges the valuable comments and constructive suggestions by the anonymous referee that lead to a significant improvement of the manuscript. TCH is thankful to David Asher, Matija Ćuk and Mark Bailey for fruitful discussions and to Julien Frouard for sharing early results on the dynamics of Jovian irregular satellites. Also the authors would like to thank Anthony R. Dobrovolskis for suggestions and improving the readability of the original manuscript. Numerical simulations have been performed on the supercomputing facility at the University of Copenhagen (DCSC-KU) run on behalf of the Danish Centre for Scientific Computing and the SFI/HEA Irish Centre for High-End Computing (ICHEC). TCH is thankful to Aake Nordlund for providing access to the (DCSC-KU) computing facility. Astronomical research at the Armagh Observatory is funded by the Northern Ireland Department of Culture, Arts and Leisure (DCAL).

## REFERENCES

- Barrio R., Borczyk W., Breiter S., 2009, Chaos, Solitons Fractals, 40, 1697  
 Benettin G., Galgani L., Strelcyn J.-M., 1976, Phys. Rev. A, 14, 2338  
 Benettin G., Galgani L., Giorgilli A., Strelcyn J.-M., 1980, Meccanica, 15, 9  
 Bois E., Kiseleva-Eggleton L., Rambaux N., Pilat-Lohinger E., 2003, ApJ, 598, 1312  
 Breiter S., Melendo B., Bartczak P., Wytrzyszczak I., 2005, A&A, 437, 753  
 Canup R. M., Ward W. R., 2002, AJ, 124, 3404  
 Carpino M., Milani A., Nobili A., 1987, A&A, 181, 182  
 Carruba V., Burns J., Nicholson P., Gladman B., 2002, Icarus, 158, 434  
 Chambers J., 1999, MNRAS, 304, 793  
 Chambers J., Migliorini F., 1997, BAAS, 29, 1024  
 Christou A. A., 2005, Icarus, 174, 215  
 Cincotta P., Simó C., 1999, Celest. Mech. Dynamical Astron., 73, 195  
 Cincotta P., Simó C., 2000, ApJS, 147, 205  
 Cincotta P., Giordano C., 2004, A&A, 423, 745  
 Cincotta P., Giordano C., Simó C., 2003, Physica D, 182, 151  
 Ćuk M., Burns J., 2004, AJ, 128, 2518  
 Dvorak R., Freistetter F., Kurths J., eds, 2005, Lecture Notes Physics 683, Chaos and Stability in Planetary Systems. Springer Verlag, Berlin, p. 141  
 Estrada P. R., Mosquera I., 2006, Icarus, 181, 486  
 Ferraz-Mello S., 1994, AJ, 108, 2330  
 Froeschlé C., Lega E., Gonczi R., 1997, Celest. Mech. Dynamical Astron., 67, 41  
 Frouard J., Fouchard M., Vienne A., 2008, in Charbonnel C., Combes F., Samadi R., eds, Proc. SF2A 2008, Scientific Highlights. French Soc. Astron. Astrophys., p. 121 (<http://proc.sf2a.asso.fr>)  
 Gayon J., Bois E., 2008, A&A, 482, 665  
 Giorgini J. D. et al., 1996, BAAS, 28, 1158  
 Gladman B. J., Nicholson P. D., Burns J. A., Kavelaars Jj., Marsden B. G., Williams G. V., Offutt W. B., 1998, Nat, 392, 897  
 Gladman B. J., Kavelaars Jj., Holman M., Petit J.-M., Scholl H., Nicholson P., Burns J. A., 2000, Icarus, 147, 320  
 Gladman B. J. et al., 2001, Nat, 412, 163  
 Goldreich R., Rappaport N., 2003, Icarus, 166, 320  
 Goździewski K., 2002, A&A, 393, 997  
 Goździewski K., 2004, ApJ, 610, 1093  
 Goździewski K., Bois E., Maciejewski A., Kiseleva-Eggleton L., 2001, A&A, 378, 569  
 Goździewski K., Bois E., Maciejewski A. J., 2002, MNRAS, 332, 839  
 Gurzadyan V. G., Ruffini R., 2000, Proc. Second ICRA Network Workshop, The Chaotic Universe. World Scientific Publishing, Singapore  
 Haghghiipour N., Jewitt D., 2008, AJ, 136, 909  
 Hairer E., Norsett S., Wanner G., 1993, Solving Ordinary Differential Equations I. Non-stiff Problems, Springer Series in Computational Mathematics, 2nd edn. Springer-Verlag, Berlin  
 Hamilton D. P., Krivov A. V., 1997, Icarus, 128, 241  
 Holman M. J. et al., 2004, Nat, 430, 865  
 Jewitt D., Haghghiipour N., 2007, ARA&A, 45, 261  
 Laskar J., 1990, Icarus, 88, 266  
 Michtchenko T., Ferraz-Mello S., 1995, A&A, 303, 945  
 Mikkola S., Innanen K., 1999, Celest. Mech. Dynamical Astron., 74, 59  
 Milani A., Nobili A. M., 1992, Nat, 357, 569  
 Milani A., Nobili A. M., Knezevic Z., 1997, Icarus, 125, 13  
 Morbidelli A., 1997, Icarus, 127, 1  
 Morbidelli A., 2002, Modern Celestial Mechanics - Aspects of Solar System Dynamics. Taylor & Francis, London  
 Morbidelli A., Nesvorný D., 1999, Icarus, 139, 295  
 Mosquera I., Estrada P. R., 2003, Icarus, 163, 198  
 Murray C., Dermott S., 2001, Solar System Dynamics. Cambridge Univ. Press, Cambridge  
 Nesvorný D., Ferraz-Mello S., 1997, A&A, 320, 672  
 Nesvorný D., Beaugé, 2007, AJ, 133, 2537  
 Nesvorný D., Alvarellos J. L. A., Dones L., Levison H. F., 2003, AJ, 126, 398  
 Nesvorný D., Beaugé C., Dones L., 2004, AJ, 127, 1768  
 Nicholson P. D., Ćuk M., Sheppard S. S., Nesvorný D., Johnson T. V., 2008, The Solar System Beyond Neptune. Univ. Arizona Press, Tucson  
 Peale S., 1999, ARA&A, 37, 533  
 Press W., Teukolsky S. A., Vetterling W., Flannery B., 1996, Numerical Recipes in Fortran 77 – The Art of Scientific Computing. Cambridge Univ. Press, Cambridge  
 Quinn T., Tremaine S., Duncan M., 1991, AJ, 101, 2287  
 Saha P., Tremaine S., 1993, Icarus, 106, 549  
 Sándor Z., Érdi B., Széll A., Funk B., 2004, Celest. Mech. Dynamical Astron., 90, 127  
 Shen Y., Tremaine S., 2008, AJ, 136, 2453  
 Sheppard S. S., Jewitt D. C., 2003, Nat, 423, 261  
 Sheppard S. S., Jewitt D. C., Marsden B. G., 2005, Minor Planet Electron. Circular, 2005-J13  
 Sheppard S. S., Jewitt D. C., Kleyna J., 2006, Minor Planet Electron. Circular, 2006-M44, 2006-45, 2006-M48  
 Skokos C., 2008, Lecture Notes Physics, in press (arXiv:0811.0882v2)  
 Skokos C., Antonopoulos C., Bountis T. C., Vrahatis M. N., 2003, Progress Theor. Phys. Suppl., 150, 439

- Skokos C., Bountis T. C., Antonopoulos C., 2007, *Physica D*, 231, 30  
Sussman G., Wisdom J., 1988, *Sci*, 241, 433  
Tancredi G., Sánchez A., 2001, *AJ*, 121, 1171  
Tsiganis K., Varvoglis H., Hadjidemetriou J. D., 2002, *Icarus*, 159, 284  
Valk S., Delsate N., Lemaître A., Carletti T., 2009, *Adv. Space Res.*, 43,  
1509  
Whipple A. L., Shelus P. J., 1993, *Icarus*, 101, 265  
Wisdom J., 1983, *Icarus*, 56, 51

- Wolf A., Swift J. B., Swinney H. L., Vastano J. A., 1985, *Physica D*, 16, 285  
Yokoyama T., Santos M., Cardin G., Winter O., 2003, *A&A*, 401, 763  
Yokoyama T., Viera Neto E., Winter O. C., Sanchez D. M., de Oliveira Brasil  
P., 2008, *Math. Problems Eng.*, 2008, 16

This paper has been typeset from a  $\text{\TeX}/\text{\LaTeX}$  file prepared by the author.